



Institut für Numerische Simulation

Rheinische Friedrich-Wilhelms-Universität Bonn

Wegelerstraße 6 • 53115 Bonn • Germany
phone +49 228 73-3427 • fax +49 228 73-7527
www.ins.uni-bonn.de

M. Griebel, A. Rüttgers

Multiscale simulations of three-dimensional viscoelastic flows in a square-square contraction

INS Preprint No. 1313

March 2015

Multiscale simulations of three-dimensional viscoelastic flows in a square-square contraction

M. Griebel^a, A. Rüttgers^{a,*}

^a*Institute for Numerical Simulation, University of Bonn, Wegelerstr. 6, 53115 Bonn, Germany*

Abstract

We apply the multiscale FENE model to a 3D square-square contraction flow problem and to two 2D benchmark experiments. For this purpose, we couple the stochastic Brownian configuration field method (BCF) with our fully parallelized three-dimensional Navier-Stokes solver NaSt3DGP. The robustness of the BCF method enables the numerical simulation of higher Deborah number flows for which most macroscopic methods suffer from stability issues. We validate our implementation by investigating the numerical error for a 2D viscoelastic Poiseuille flow that has an analytical solution. Furthermore, we compare the FENE model with the FENE-P closure for a two-dimensional 4 : 1 contraction flow. We then compare the results of our 3D simulations with that of experimental measurements from literature and obtain a very good agreement. In particular, we are able to reproduce effects such as strong vortex enhancement, streamline divergence and flow inversion for highly elastic flows. Due to their computational complexity, our simulations require massively parallel computations. To this end, we use a domain decomposition approach with MPI.

Keywords: multiscale simulation, micro-macro method, Brownian configuration fields, FENE dumbbell, 3D contraction flow, high-performance computing

1. Introduction

The macroscopic mathematical modeling of dilute viscoelastic fluids usually involves an additional stress tensor in the Navier-Stokes equations and the solution of a differential or integral constitutive equation to compute the stress tensor entries. Here, the Oldroyd-B model can be employed. It originates from a two-bead dumbbell model with a linear Hookean spring force. Despite its shortcoming to describe extensional flows accurately, it is widely used for simulating dilute polymeric fluids. Other constitutive models for dilute polymeric fluids include the FENE-P model of Peterlin [1] and the FENE-L model of Lielens et al. [2]. Both models are simplifications, obtained with closure approximations, of a two-bead dumbbell system connected with a finitely extensible nonlinear elastic (FENE) spring. In the literature, there is no known direct constitutive model for the FENE spring so far and it is widely assumed that it does not exist. An extensive description of constitutive models is given in the book by Owens and Phillips [3].

More advanced multiscale approaches have been recently developed that directly solve the kinetic equations of the microscopic system. In this case, the macroscopic stress tensor results from the internal configurations of

the underlying molecular system. Using this ansatz avoids further closure errors but yields the mathematical problem of adequately modeling the internal orientations. Biller and Petruccione theoretically investigated this approach in their pioneering work in 1988 [4]. A detailed overview of micro-macro approaches is given in a general survey by Keunings [5].

Representing polymer molecules by a system of beads connected with massless springs leads to a high-dimensional diffusion equation, the Fokker-Planck equation, that describes the evolution of the configuration probability density function (cf. Bird et al. [6]). Then, Kramers' formula connects the stress tensor with the expectation of the instantaneous polymer configuration. Even for a simple dumbbell system, the Fokker-Planck equation for non-homogeneous, three-dimensional flow systems is six-dimensional. Three dimensions are needed for the physical space of the flow system and three dimensions are needed to describe the dumbbell's internal orientation which is referred to as configuration space. More complex multi-bead systems involve configuration spaces of higher dimensionality and require special numerical treatment to reduce the curse of dimensionality. Chauvière and Lozinski [7] proposed a first-order operator splitting of the Fokker-Planck equation to separate operator treatment in the physical space from that of the configuration space [8, 9]. They applied their spectral method approach to two- and three-dimensional configuration spaces and non-homogeneous two-dimensional physical spaces. Recently, Knezevic and Süttgers

*Corresponding author. Tel.: +49 228 733170; fax: +49 228 737527

Email addresses: griebel@ins.uni-bonn.de (M. Griebel), ruettgerts@ins.uni-bonn.de (A. Rüttgers)

li [10] used a similar technique that is based on a spectral Galerkin discretization with weighted ansatz and test functions in configuration space and a three-dimensional finite element discretization in physical space. A promising new approach to deal with configuration spaces of up to twenty dimensions is the Proper Generalized Decomposition (PGD) method (cf. Chinesta et al. [11]). So far, the solution in high-dimensional configuration spaces with the PGD approach has been primarily applied to homogeneous flow problems that are simple in the flow space. The most advanced implementation which we are aware of is a two-dimensional contraction flow problem considered in Mokdad et al. [12].

A more common method for multiscale viscoelastic flow simulations is based on the theory of stochastic calculus. The main idea is to rewrite the Fokker-Planck equation as a formally equivalent stochastic differential equation in which a Wiener process models the Brownian forces acting on the polymer. Numerical treatment of stochastic differential equations normally leads to stochastic noise in the stress tensor solution. On the other hand, stochastic approaches are more adapted to higher Weissenberg or Deborah number flows than comparable methods as noted by Mangoubi et al. [13]. Furthermore, they are, due to their intrinsic Monte-Carlo method, less affected by the curse of dimensionality than deterministic Fokker-Planck based methods in high-dimensional configuration spaces.

In 1993, Laso and Öttinger [14] introduced the particle-based CONNFFESSIT method (**C**alculation of **N**on-**N**ewtonian **F**low: **F**inite **E**lements and **S**tochastic **S**imulation **T**echniques) and applied it to two-dimensional flow problems. In this approach, a large number of sample particles in the flow domain approximates the stochastic process numerically. Each particle, representing a polymeric configuration, moves within the physical flow domain. Using Monte-Carlo integration, we obtain the stress tensor as the first moment of the particle orientations. However, the method exhibits several shortcomings such as wild spatial fluctuation of the stress tensor which is caused by a non-uniform particle density and uncorrelated Brownian forces acting on individual sample particles (cf. Lozininski et al. [15]).

A different stochastic approach, the Brownian configuration field (BCF) method by Hulsen et al. [16], significantly reduces the drawbacks of CONNFFESSIT by using an Eulerian particle description. The BCF method uses a uniform number of configuration fields at fixed spatial positions to ensure a homogeneous polymeric density in physical space. Furthermore, it assumes locally correlated Brownian forces which leads to a uniform stress tensor field in the flow space. According to Bonvin and Picasso [17], this simplification might reduce the global accuracy of the stress tensor field. On the other hand, the spatial smoothness of the BCF method leads to a considerably increased stability of the numerical scheme.

Multiscale simulations involve an increased computational effort compared to purely macroscopic approaches.

Therefore, most micro-macro simulations are so far restricted to homogeneous flow fields or two-dimensional physical spaces (cf. Vargas et al. [18], Prieto et al. [19], Koppol et al. [20, 21] and Smith and Sequeira [22]). To the best of our knowledge, Ramírez and Laso [23] performed the first three-dimensional stochastic BCF simulations and only recently Knezevic and Süli [10] accomplished the first three-dimensional simulation for a coupled Fokker-Planck and Stokes flow system. In both cases, the authors parallelized their algorithms to reduce computing time.

In the following, we present the first 3D multiscale FENE simulations using the BCF approach for square-square contraction flows and compare our results with that from laboratory experiments. Our multiscale simulations are more stable than comparable macroscopic flows with high Deborah numbers.

The remainder of this article is organized as follows: First, we consider the governing equations on the macro- and micro-scale in Section 2. We then describe adequate initial conditions for the stochastic equations in the case of a Hookean and a FENE dumbbell system. In Section 3 we discuss spatial and temporal discretization schemes of the Navier-Stokes, Oldroyd-B and stochastic differential equations. Furthermore, we describe our domain decomposition approach to enable parallel computation using MPI and consider variance reduction techniques. In Section 4.1, we investigate the numerical error for a 2D viscoelastic Poiseuille flow that has an analytical solution in the Oldroyd-B/Hookean dumbbell case. We then consider two-dimensional contraction flows for the FENE and FENE-P model in Section 4.2 for which published simulation results are available. Moreover, we present the results of 3D square-square contraction flows in Section 4.3 and compare them with those from literature. At last, we evaluate our findings and discuss possible extensions.

2. Governing equations for the micro-macro model

Throughout this article, we consider fluid flow in a bounded domain $\Omega \subset \mathbb{R}^3$ and refer to Ω as physical space. For any position $\mathbf{x} \in \Omega$ and any time $t \in (0, T] \in \mathbb{R}$, the fluid velocities $\mathbf{u}(\mathbf{x}, t) \in \mathbb{R}^3$ and the hydrodynamic pressure $p(\mathbf{x}, t) \in \mathbb{R}$ combined with appropriate boundary conditions fully describe the current state of a purely Newtonian system. We first give the Navier-Stokes and the stress tensor equations on the macro-scale. Subsequently, we specify the alternative stress tensor approaches on the micro-scale that either involve a Fokker-Planck or a stochastic differential equation.

2.1. Macroscopic equations

On the macroscopic scale, conservation of momentum and mass for an incompressible and isothermal viscoelastic

one-phase flow is given by the coupled system of equations

$$\rho \left(\frac{\partial \mathbf{u}}{\partial t} + \mathbf{u} \cdot \nabla \mathbf{u} \right) = -\nabla p + \eta_s \Delta \mathbf{u} + \nabla \cdot \boldsymbol{\tau}_p \quad (1)$$

$$\nabla \cdot \mathbf{u} = 0 \quad (2)$$

with $\rho \in \mathbb{R}^+$ as the fluid density, $\eta_s \in \mathbb{R}^+$ as solvent viscosity, and $\boldsymbol{\tau}_p$ as the second-order tensor for the polymeric stress contribution.

These equations are coupled with initial conditions

$$\begin{aligned} \mathbf{u}(\mathbf{x}, 0) &= \mathbf{u}_0(\mathbf{x}), \\ p(\mathbf{x}, 0) &= p_0(\mathbf{x}), \\ \boldsymbol{\tau}_p(\mathbf{x}, 0) &= \boldsymbol{\tau}_0(\mathbf{x}) \quad \forall \mathbf{x} \in \Omega, \end{aligned}$$

with one of the following conditions for the velocity field on the boundary $\partial\Omega = \Gamma_1 \cup \Gamma_2 \cup \Gamma_3$

$$\begin{aligned} \mathbf{u}|_{\Gamma_1} &= \mathbf{u}_0 && \text{inflow boundary } \Gamma_1, \\ \mathbf{u}|_{\Gamma_2} &= 0 && \text{no-slip boundary } \Gamma_2, \\ \partial_{\mathbf{n}}(\mathbf{u} \cdot \mathbf{n})|_{\Gamma_3} &= 0, \quad \partial_{\mathbf{n}}(\mathbf{u} \cdot \mathbf{t})|_{\Gamma_3} = 0 && \text{outflow boundary } \Gamma_3. \end{aligned}$$

Here, \mathbf{n} denotes the outward pointing unit normal and \mathbf{t} denotes the tangential vector on $\partial\Omega$, respectively.

On the macro-scale we consider the Oldroyd-B model. It is equivalent to a Hookean dumbbell system on the micro-scale. First, for an arbitrary second-order tensor \mathbf{A} we define the upper convected derivative or Oldroyd derivative as

$$\overset{\nabla}{\mathbf{A}} \equiv \frac{\partial \mathbf{A}}{\partial t} + (\mathbf{u} \cdot \nabla) \mathbf{A} - \nabla \mathbf{u} \cdot \mathbf{A} - \mathbf{A} \cdot (\nabla \mathbf{u})^T.$$

Then, the Oldroyd-B model takes the form

$$\boldsymbol{\tau}_p + \lambda \overset{\nabla}{\boldsymbol{\tau}}_p = 2\eta_p \mathbf{D} \quad (3)$$

with the symmetric deformation tensor

$$\mathbf{D} = \frac{1}{2}(\nabla \mathbf{u} + (\nabla \mathbf{u})^T),$$

λ the relaxation time of the dumbbell system and η_p the zero shear rate polymeric viscosity.

We rewrite equations (1), (2) and (3) in a dimensionless form by scaling the equations with the characteristic units L_c (characteristic length in macroscopic flow), U_c (characteristic fluid velocity), ρ_c (fluid density, scaling pressure term with $1/(\rho U_c^2)$) and we normalize the polymeric stress tensor with $L_c/(U_c(\eta_s + \eta_p))$. This yields the following dimensionless system of equations

$$\frac{\partial \mathbf{u}}{\partial t} + \mathbf{u} \cdot \nabla \mathbf{u} = -\nabla p + \frac{1}{Re} \beta \Delta \mathbf{u} + \frac{1}{Re} \nabla \cdot \boldsymbol{\tau}_p \quad (4)$$

$$\nabla \cdot \mathbf{u} = 0 \quad (5)$$

$$\boldsymbol{\tau}_p + De \overset{\nabla}{\boldsymbol{\tau}}_p = 2(1 - \beta) \mathbf{D} \quad (6)$$

which involve the dimensionless parameters De (Deborah number), Re (Reynolds number) and β (viscosity ratio). They are defined as

$$Re = \frac{\rho_c U_c L_c}{\eta_s + \eta_p}, \quad De = \frac{\lambda U_c}{L_c}, \quad \beta = \frac{\eta_s}{\eta_s + \eta_p}. \quad (7)$$

Note that (6) reduces to the Upper-Conveyed Maxwell equation for $\beta \rightarrow 0$. For simplicity, we have used the same notation for the unknowns in the dimensionless formulation as in (1)–(3).

2.2. Microscopic equations

On the microscopic scale, we employ a dumbbell model for approximating a dilute polymeric fluid, immersed in a Newtonian solvent. It consists of two separate masses connected with an elastic spring. The spring denotes intermolecular forces between both beads. For a complete description we require the dumbbell's position in the flow domain $\mathbf{x} \in \Omega$ as well as the orientation of the bead's end-to-end vector $\mathbf{q} \in D \subseteq \mathbb{R}^3$. We refer to D as configuration space.

2.2.1. Deterministic Fokker-Planck approach

Let $\psi : \Omega \times D \times [0, T] \rightarrow \mathbb{R}^+$, $(\mathbf{x}, \mathbf{q}, t) \mapsto \psi(\mathbf{x}, \mathbf{q}, t)$ denote the probability of finding dumbbells at time t with a position in $[\mathbf{x}, \mathbf{x} + d\mathbf{x}]$ and an orientation vector in $[\mathbf{q}, \mathbf{q} + d\mathbf{q}]$. ψ is a probability density function (pdf) and fulfills

$$\begin{aligned} \psi(\mathbf{x}, \mathbf{q}, t) &\geq 0 && \forall (\mathbf{x}, \mathbf{q}, t) \in \Omega \times D \times [0, T] \\ \int_D \psi(\mathbf{x}, \mathbf{q}, t) d\mathbf{q} &= 1 && \forall (\mathbf{x}, t) \in \Omega \times [0, T]. \end{aligned}$$

The application of Newton's second law to the forces acting on a dumbbell system (hydrodynamic drag force, spring force and Brownian forces) leads to the dimensionless Fokker-Planck equation

$$\begin{aligned} \frac{\partial \psi}{\partial t} + \nabla_{\mathbf{x}} \cdot (\mathbf{u} \psi) + \nabla_{\mathbf{q}} \cdot \left((\nabla_{\mathbf{x}} \mathbf{u})^T \mathbf{q} \psi \right. \\ \left. - \frac{1}{2 De} \mathbf{F}(\mathbf{q}) \psi \right) = \frac{1}{2 De} \Delta_{\mathbf{q}} \psi. \quad (8) \end{aligned}$$

It describes the evolution of ψ under the dumbbell's spring force $\mathbf{F} : \mathbb{R}^3 \rightarrow \mathbb{R}^3$. In (8) we have dropped the diffusion $\Delta_{\mathbf{x}} \psi$ in physical space since the diffusion coefficient scales quadratically in the micro-macro length scale ratio L_c/l_c and is usually only of the order 10^{-8} according to Bhave et al. [24].

We employ three different spring forces for the characterization of intermolecular forces defined as

$$\mathbf{F}(\mathbf{q}) = \mathbf{q}, \quad \mathbf{q} \in \mathbb{R}^3 \quad (\text{Hooke}), \quad (9)$$

$$\mathbf{F}(\mathbf{q}) = \frac{\mathbf{q}}{1 - \|\mathbf{q}\|^2/b}, \quad \|\mathbf{q}\|^2 \leq b \quad (\text{FENE}), \quad (10)$$

$$\mathbf{F}(\mathbf{q}) = \frac{\mathbf{q}}{1 - \langle \mathbf{q}^2 \rangle / b}, \quad \langle \mathbf{q}^2 \rangle \leq b \quad (\text{FENE-P}) \quad (11)$$

with $b = \|\mathbf{q}_{\max}\|^2/l_c$ as dimensionless unit for the dumbbell's maximum extension \mathbf{q}_{\max} compared to a characteristic micro length l_c . For the Hookean spring force (9), we observe that the dumbbell's extension is not restricted which leads to unbounded stress tensor values for certain types of extensional flows. In an analogous way, only the

average dumbbell length $\langle \mathbf{q}^2 \rangle = \int_D \mathbf{q}^2 \psi(\mathbf{x}, \mathbf{q}, t) d\mathbf{q}$ is restricted for the FENE-P spring. Consequently, the FENE-P model also leads to spring extensions that exceed a maximum length of \sqrt{b} and to \mathbb{R}^3 as configuration space. The FENE spring differs from this with the configuration space D being a sphere with radius \sqrt{b} around the origin, i.e. $D = B(0, \sqrt{b})$.

The pdf ψ in (8) represents the polymeric configurations of the micro-system. Now, Kramers' expression couples the internal configurations to the macroscopic stress tensor by

$$\boldsymbol{\tau}_p = \frac{\alpha_{b,d}(1-\beta)}{De} (\langle \mathbf{q} \otimes \mathbf{F}(\mathbf{q}) \rangle - \mathbf{Id}) \quad (12)$$

where $\langle \cdot \rangle = \int_D \cdot \psi(\mathbf{x}, \mathbf{q}, t) d\mathbf{q}$ denotes the expectation in configuration space. The prefactor $\alpha_{b,d}$ specifies a spring dependent constant and is defined as

$$\alpha_{b,d} \equiv \begin{cases} 1, & \text{for Hookean dumbbells } (b \rightarrow \infty), \\ \frac{b+5}{b}, & \text{for 3-dimensional FENE dumbbells,} \\ \frac{b+3}{b}, & \text{for 3-dimensional FENE-P dumbbells.} \end{cases}$$

Due to conservation of angular momentum, $\boldsymbol{\tau}_p$ is symmetric. Inserting the spring forces (9) – (11) into (12) results in the symmetry condition for $\boldsymbol{\tau}_p$.

2.2.2. Stochastic Brownian configuration field approach

The BCF method employs a formal equivalence between the Fokker-Planck equation and a corresponding stochastic differential equation. To this end, we rewrite (8) as

$$d\mathbf{Q}_t(\mathbf{x}) = \left(-\mathbf{u} \nabla \mathbf{Q}_t(\mathbf{x}) + (\nabla_{\mathbf{x}} \mathbf{u})^T \mathbf{Q}_t(\mathbf{x}) - \frac{1}{2 De} \mathbf{F}(\mathbf{Q}_t(\mathbf{x})) \right) dt + \sqrt{\frac{1}{De}} d\mathbf{W}_t. \quad (13)$$

This describes the evolution of a stochastic process \mathbf{Q}_t that represents the configuration vector \mathbf{q} . We model Brownian forces by a three-dimensional Wiener process \mathbf{W}_t . As \mathbf{W}_t is a Gaussian process, we fully describe it by its first and second moments $\langle \mathbf{W}_t \rangle = 0$ and $\langle \mathbf{W}_t \mathbf{W}_{t'} \rangle = \min(t, t') \mathbf{Id}$. We solve (13) for a number of $i = 1, \dots, N_{BCF}$ stochastic realizations $\mathbf{Q}_t^{(i)}$, the Brownian configuration fields, which are distributed according to the density function ψ . The convective term $-\mathbf{u} \nabla \mathbf{Q}_t$ in (13) represents the transport of the spatially fixed configuration fields through Ω . Furthermore, the BCF method assumes correlated Wiener processes at different points in Ω such that \mathbf{W}_t does not depend on \mathbf{x} . This leads to a smooth stress tensor field in space.

Since we do not know the actual density ψ , we approximate the first moment $\langle \mathbf{Q}_t \otimes \mathbf{F}(\mathbf{Q}_t) \rangle$ in Kramers' relation (12) as

$$\boldsymbol{\tau}_p \approx \frac{\alpha_{b,d}(1-\beta)}{De} \left(\frac{1}{N_{BCF}} \sum_{i=1}^{N_{BCF}} \mathbf{Q}_t^{(i)} \otimes \mathbf{F}(\mathbf{Q}_t^{(i)}) - \mathbf{Id} \right), \quad (14)$$

i.e. we replace the integral by a MC quadrature formula. One drawback of Monte Carlo integration is the low order $\mathcal{O}(N_{BCF}^{-1/2})$ for the error reduction in $\boldsymbol{\tau}_p$. The accuracy of $\boldsymbol{\tau}_p$ as well as the computing time critically depends on the choice of N_{BCF} . This underlines the importance of parallelization in 3D multiscale simulations to obtain sufficiently small relative errors in $\boldsymbol{\tau}_p$ for a reasonable amount of computing time.

2.2.3. Initial condition for the density function

The initial configuration fields $\mathbf{Q}_0^{(i)}$ are distributed according to the equilibrium solution $\psi_{eq}(\mathbf{q})$ of the Fokker-Planck equation, i.e. according to the solution of the Fokker-Planck equation for the velocity field $\mathbf{u} = 0$ in Ω . In this case (8) simplifies to

$$-\nabla_{\mathbf{q}} \cdot (\mathbf{F}(\mathbf{q}) \psi_{eq}(\mathbf{q})) = \Delta_{\mathbf{q}} \psi_{eq}(\mathbf{q}). \quad (15)$$

The gauged equilibrium solutions, presented in the form of Bonvin [25] and Herrchen and Öttinger [26], respectively, are

$$\psi_{eq}(\mathbf{q}) = \frac{1}{(2\pi)^{3/2}} \exp\left(-\frac{\|\mathbf{q}\|^2}{2}\right) \quad (\text{Hooke}), \quad (16)$$

$$\psi_{eq}(\mathbf{q}) = \frac{1}{2\pi b^{3/2} \mathcal{B}(\frac{3}{2}, \frac{b+2}{2})} \left(1 - \frac{\|\mathbf{q}\|^2}{b}\right)^{b/2} \quad (\text{FENE}), \quad (17)$$

$$\psi_{eq}(\mathbf{q}) = \left(\frac{b+3}{2\pi b}\right)^{3/2} \exp\left(-\frac{b+3}{2b} \|\mathbf{q}\|^2\right) \quad (\text{FENE-P}). \quad (18)$$

The gauging of Kramers' expression ensures a stress tensor value of zero for ψ_{eq} . The denominator in (17) includes the beta function $\mathcal{B}(.,.)$ that is defined by

$$\mathcal{B}(x, y) = \int_0^1 s^{x-1} (1-s)^{y-1} ds \quad \text{for } x, y > 0.$$

Considering the Gaussian equilibrium distribution in (16) for which we have zero mean and a covariance matrix \mathbf{Id} , one could think of using various conventional random number generators to generate $\mathbf{Q}_0^{(i)}$. However, since the FENE density (17) is not Gaussian, we have to generate appropriate random numbers by other means. To this end, we employ the rejection sampling/acceptance-rejection method proposed by von Neumann [27]. It requires a comparison function. We decided here for the uniform density $U : B(0, \sqrt{b}) \rightarrow \mathbb{R}^+$, $\mathbf{q} \mapsto 3/(4\pi b^{3/2})$. Furthermore, we need a constant M such that $\psi_{eq}(\mathbf{q}) \leq MU(\mathbf{q})$ for all $\mathbf{q} \in D$. The optimal choice for M in our case is

$$M_{opt} = \frac{\psi(0)}{U(0)} = \frac{2}{3\mathcal{B}(\frac{3}{2}, \frac{b+2}{2})}.$$

3. Numerical discretization

We subsequently describe the coupling of the Oldroyd-B and the microscopic models with our three-dimensional

Navier-Stokes solver NaSt3DGPF [28, 29]. First, we consider the spatial and temporal discretization, then we describe the parallelization approach and at last we discuss the applied variance reduction scheme.

3.1. Spatial discretization

For the discretization of the Navier-Stokes equations (4) and (5) in Ω , we use a finite difference scheme. For this purpose, we subdivide Ω into N_g rectangular grid cells and evaluate the macroscopic unknowns $\mathbf{u}, p, \boldsymbol{\tau}_p$ on a staggered grid. Here, scalar values are stored in the cell centers and components of vector-valued variables, such as the three components of \mathbf{u} , are placed on the cell faces. This ensures a sufficient coupling between the pressure and the velocity field and avoids numerical instability. Furthermore, we place the discrete second-order tensor $\boldsymbol{\tau}_p$ in the cell centers and do not distribute the stress components on different cell faces. This reduces computation time for the multi-scale approach as each component of $\boldsymbol{\tau}_p$ requires the total number of configuration fields for its computation.

Using second-order central differences on a staggered grid, we discretize all spatial derivatives except for the convective velocity terms. For the discretization of the convective terms in the momentum equations (4), we employ a 5th-order WENO scheme [30] to minimize oscillatory solutions. The WENO scheme requires grid point information from three different adjacent positions in each coordinate direction. A similar approach is used for the Oldroyd-B constitutive equation (6). Again, we discretize the convective contributions (i.e. $(\mathbf{u} \cdot \nabla) \boldsymbol{\tau}_p$) with a 5th-order WENO scheme and apply central differences for the other terms. A more detailed description of the spatial discretization in NaSt3DGPF is given in Griebel et al. [28] and Croce et al. [29]. Furthermore, the implementation of the second-order tensor $\boldsymbol{\tau}_p$ and the Oldroyd-B and Phan-Thien Tanner model in NaSt3DGPF is described in detail in Claus [31].

On the micro-scale, we employ a set of N_{BCF} stochastic samples $\mathbf{Q}_t^{(i)}(\mathbf{x}_j)$, $i = 1, \dots, N_{BCF}$ for each discrete stress tensor value $\boldsymbol{\tau}_p(\mathbf{x}_j)$, $j = 1, \dots, N_g$ in physical space. The total number of samples for approximating the stress field in Ω is then $N_{BCF} \cdot N_g$. Furthermore, we discretize the convective part of the stochastic equation (13) with a 2nd-order QUICK scheme. The QUICK scheme requires fluid information from two neighboring cells in each coordinate direction.

The boundary conditions for the stochastic samples on $\partial\Omega$ depend on the chosen type. Using the boundary specifications of Section 2.1, we set

$$\begin{aligned} \mathbf{Q}^{(i)}(\mathbf{x})|_{\Gamma_1} &= \mathbf{Q}_0^{(i)} && \text{on the inflow boundary } \Gamma_1, \\ \nabla_{\mathbf{x}} \mathbf{Q}^{(i)}(\mathbf{x})|_{\Gamma_{2,3}} &= 0 && \text{on } \Gamma_2 \text{ and } \Gamma_3 \end{aligned}$$

for all $i = 1, \dots, N_{BCF}$ realizations in Section 4.3. We prescribe Dirichlet boundary conditions on the inflow domain from outside of the domain Ω , i.e. before the fluid enters

Ω . One approach to compute $\mathbf{Q}_0^{(i)}$ is to pre-process two-dimensional simulations with an analytically prescribed velocity field \mathbf{u}_0 on the domain Γ_1 . Using this two-dimensional flow field, we evolve a discrete set of configuration fields $\mathbf{Q}^{(i)}(\mathbf{x}_j)|_{\Gamma_1}$ from equilibrium towards steady state. For the actual three-dimensional simulation, we then set \mathbf{u}_0 as velocity profile on the inflow domain Γ_1 and reuse the steady state configuration fields as inflow fields $\mathbf{Q}_0^{(i)}$. It is crucial to reuse the same number N_{BCF} of stochastic samples as well as the same Gaussian random numbers for evolving the configuration fields towards a steady state (cf. the Euler-Maruyama scheme in Section 3.2) to ensure that $\mathbf{Q}_0^{(i)}$ represents an adequate inflow field.

3.2. Temporal discretization

We apply an implicit 2nd-order Crank-Nicolson scheme for the diffusive terms in the momentum equations (4) to reduce CFL-type restrictions in time-step size for the laminar flow regime considered in our simulations. We treat the convective velocities explicitly by employing a 2nd-order Adams-Basforth method. The ansatz is implicit in the pressure term as proposed by Bell et al. [32]. The implementation into NaSt3DGPF is described in Verleye et al. [33].

A canonic time discretization scheme for stochastic differential equations is the explicit Euler-Maruyama method. Though it is only a first order scheme, it does not restrict the accuracy of the stress tensor result for the time-step widths that are used in our simulations. The accuracy is primarily limited by the chosen number of configuration fields N_{BCF} as the sampling error dominates the temporal error. We therefore employ the explicit Euler scheme for the Hookean (9) and for the FENE-P (11) spring force.

For the FENE spring force (10), however, the explicit Euler-Maruyama method might lead to non-physical solutions since the scheme does not necessarily preserve $\|\mathbf{q}\|^2 \leq b$ as requested. A solution proposed by Öttinger [34] employs an implicit treatment of the spring force. The only unknown for solving the linear system of equations in this case is the dumbbell's extension in the new time-step, i.e. we have to determine $\|\mathbf{q}(t^{n+1})\|$. The extension is found by taking absolute values on both sides of the stochastic equation and by solving a cubic equation for $\|\mathbf{q}(t^{n+1})\|$ which has only one solution in D .

Altogether, let $\mathbf{u}^n, p^n, \boldsymbol{\tau}_p^n$ and \mathbf{Q}_n denote the discretized variables at time $t^n \in [0, T]$. Then, the method for computing $t^n + \Delta t^n = t^{n+1} \in (0, T]$ consists of the following steps:

1. In case of the Hookean and the FENE-P spring forces (9) and (11), respectively, we solve the Brownian configuration field equation for $j = 1, \dots, N_g$ grid cells and for $i = 1, \dots, N_{BCF}$ configuration fields by using the

explicit Euler-Maruyama method

$$\begin{aligned}\mathbf{Q}_{n+1}^{(i)}(\mathbf{x}_j) &= \mathbf{Q}_n^{(i)}(\mathbf{x}_j) + \left(-\mathbf{u}^n \nabla \mathbf{Q}_n^{(i)}(\mathbf{x}_j) \right. \\ &\quad \left. + (\nabla_{\mathbf{x}} \mathbf{u}^n)^T \mathbf{Q}_n^{(i)}(\mathbf{x}_j) - \frac{1}{2 De} \mathbf{F}(\mathbf{Q}_n^{(i)}(\mathbf{x}_j)) \right) \\ &\quad \Delta t^n + \sqrt{\frac{\Delta t^n}{De}} \mathbf{N}(0, 1)^{(i)}.\end{aligned}$$

In case of the FENE spring force, we employ the semi-implicit Euler method

$$\begin{aligned}\left(1 + \frac{\Delta t^n}{2 De (1 - \|\mathbf{Q}_{n+1}^{(i)}\|^2/b)} \right) \mathbf{Q}_{n+1}^{(i)}(\mathbf{x}_j) &= \mathbf{Q}_n^{(i)}(\mathbf{x}_j) \\ &+ \left(-\mathbf{u}^n \nabla \mathbf{Q}_n^{(i)}(\mathbf{x}_j) + (\nabla_{\mathbf{x}} \mathbf{u}^n)^T \mathbf{Q}_n^{(i)} \right) \\ &\quad \Delta t^n + \sqrt{\frac{\Delta t^n}{De}} \mathbf{N}(0, 1)^{(i)}.\end{aligned}$$

In both cases, $\mathbf{N}(0, 1)$ denotes a triple of independent Gaussian random variables with zero mean and variance one.

2. We compute the new stress tensor using Kramers' expression, i.e. we set

$$\begin{aligned}\boldsymbol{\tau}_p^{n+1}(\mathbf{x}_j) &= \frac{\alpha_{b,d}(1-\beta)}{De} \left(\frac{1}{N_{BCF}} \sum_i \mathbf{Q}_{n+1}^{(i)}(\mathbf{x}_j) \right. \\ &\quad \left. \otimes \mathbf{F}(\mathbf{Q}_{n+1}^{(i)}(\mathbf{x}_j)) - \mathbf{Id} \right).\end{aligned}$$

3. We solve a Helmholtz equation to calculate an intermediate velocity field \mathbf{u}^*

$$\begin{aligned}\left(\mathbf{Id} - \frac{\Delta t^n \beta}{2 Re} \right) \mathbf{u}^* &= \mathbf{u}^n - \Delta t^n \left(\nabla p^n + \mathbf{u}^n \cdot \nabla \mathbf{u}^n \right. \\ &\quad \left. - \frac{\beta}{2 Re} \Delta \mathbf{u}^n - \frac{1}{Re} \nabla \cdot \boldsymbol{\tau}_p^{n+1} \right)\end{aligned}$$

by using an SSOR preconditioned CG method.

4. We use \mathbf{u}^* on the right hand side of a Poisson problem to compute a pressure correction ϕ^{n+1} and recover \mathbf{u}^{n+1} , i.e.

$$\begin{aligned}\Delta \phi^{n+1} &= \frac{1}{\Delta t^n} \nabla \cdot \mathbf{u}^* \\ \mathbf{u}^{n+1} &= \mathbf{u}^* - \Delta t^n \nabla \phi^{n+1}.\end{aligned}$$

5. We obtain the new pressure field by computing

$$p^{n+1} = p^n + \phi^{n+1} - \frac{\Delta t^n \beta}{2 Re} \Delta \phi^{n+1}.$$

3.3. Parallelization

We encounter the following two problems in multiscale flow simulations with a total number of $N_g N_{BCF}$ configuration fields which emphasize the need of parallelization:

1. Solving $N_g N_{BCF}$ stochastic differential equations per time-step demands large computing times to solve physical systems of interest.

2. A large number of stochastic realizations leads to high memory requirements. For instance, using 80^3 grid cells with $N_{BCF} = 4000$ fields per cell leads to a memory requirement of about 50 GB in double precision accuracy.

A natural approach for parallelization is to employ domain decomposition, see also Smith et al. [35]. There, we partition the physical space Ω into subdomains $\Omega_1, \dots, \Omega_N$ and assign the local data and operations to different processors. Processors whose subdomains share a common boundary have to exchange data with each other in the overall algorithm when necessary. Details of the data exchange for the macroscopic variables in NaSt3DGPF can be found in Croce et al. [36].

Exchanging the BCFs is by far the most CPU intensive part of the parallel algorithm. Note that it is not necessary to exchange polymeric stress tensor values in our multiscale simulations since these values directly depend on the configuration fields.

We investigate the parallel code performance of our implementation in a test simulation. The problem is discretized with $N_g = 520 \times 128 \times 128$ grid cells and employs $N_{BCF} = 1200$ samples per grid cell for a flow with Deborah number $De = 100$. For this purpose, we perform the first 30 time steps of the semi-implicit Crank-Nicolson method on our parallel cluster *Siebengebirge*. After 30 time-steps, NaSt3DGPF has simulated a process time of about 0.02.

The HPC cluster *Siebengebirge* has 5 Dell PowerEdge R910 computing nodes with 160 Intel Xeon X7560 2.226 GHz CPU cores and a main memory of 2560 GB in total, i.e. one computing node contains 32 CPU cores and has 512 GB main memory. MPI communication on *Siebengebirge* is performed with Mellanox ConnectX Infiniband. The Linpack performance of the system is 1349 GFlops/s with a parallel efficiency of 93%.

The simulations were performed with $n = 1, 2, 4, 5$ computing nodes of the cluster *Siebengebirge*. We always used all 32 cores per node. The results of our speed-up measurements are listed in Tab. 1. The table first shows a decrease in parallel efficiency when switching from one computing node $n = 1$ to two computing nodes $n = 2$. This is due to the communication process that becomes far more expensive when the code is extended to a second node as the main memory is not separated on one node. On four or five computing nodes the parallel efficiency becomes much better since the gain in computing speed outweighs the communication effort. On five computing nodes we recover a parallel efficiency of 92%. The high parallel efficiency results from the large number of stochastic sample particles in the simulation that can be parallelized efficiently.

Table 1: Parallel code performance on CPU cluster.

#cores	#nodes	time [s]	speedup	efficiency
32	1	13531	1.0	100 %
64	2	7693	1.76	88 %
128	4	3726	3.63	91 %
160	5	2937	4.61	92 %

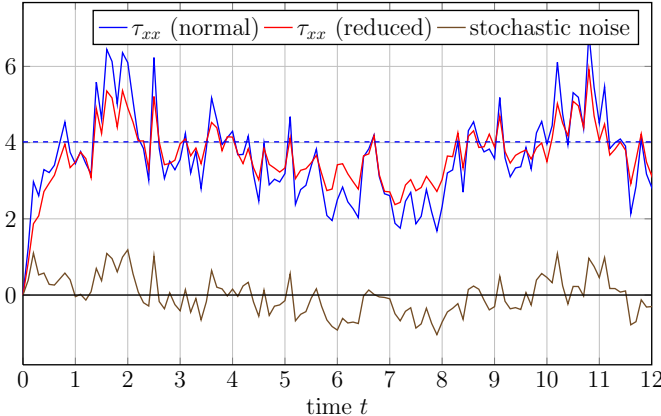


Figure 1: Plot of the τ_{xx} stress component with $N_{BCF} = 100$ for a homogeneous extensional flow (i.e. $N_g = 1$). The analytical solution for τ_{xx} at steady state is ≈ 4.02 .

3.4. Variance reduction

A variance reduction scheme decreases the variance of a stochastic simulation without increasing the computational effort. One method for variance reduction is given by *control variates*. In this approach, instead of directly computing $\langle \mathbf{Q}_t \otimes \mathbf{F}(\mathbf{Q}_t) \rangle$ in (12), we decompose the expression according to

$$\begin{aligned} \langle \mathbf{Q}_t \otimes \mathbf{F}(\mathbf{Q}_t) \rangle &= \langle \mathbf{Q}_t \otimes \mathbf{F}(\mathbf{Q}_t) - \mathbf{Y}_t \otimes \mathbf{F}(\mathbf{Y}_t) \rangle \\ &\quad + \langle \mathbf{Y}_t \otimes \mathbf{F}(\mathbf{Y}_t) \rangle. \end{aligned} \quad (19)$$

using an additional control process \mathbf{Y}_t . The basic principle is to decide for \mathbf{Y}_t such that the last term in (19) can be computed deterministically without any variance. Furthermore, the stochastic processes \mathbf{Q}_t and \mathbf{Y}_t have to be coupled strongly to reduce the variance in (19).

We reduce the variance of our simulations in Section 4 with an *equilibrium control variate* (cf. Melchior and Öttinger [37]). In this case, we reuse the same initial distribution for \mathbf{Y}_t but evolve \mathbf{Q}_t according to a simplified stochastic differential equation. For this purpose, we set $\mathbf{u} = 0$ in (13) such that \mathbf{Y}_t remains an equilibrium distribution for all time (i.e. the stress tensor contribution for \mathbf{Y}_t remains zero). Since we apply the same Brownian forces on both processes, we relate the noise in \mathbf{Y}_t to the noise in \mathbf{Q}_t .

We demonstrate the principle of an equilibrium control variate in Fig. 1 for a homogeneous extensional flow test problem. Here, we intentionally used only a few number of configurations fields, i.e. $N_{BCF} = 100$, to emphasize the

improvement. The red line, representing $\langle \mathbf{Q}_t \otimes \mathbf{F}(\mathbf{Q}_t) - \mathbf{Y}_t \otimes \mathbf{F}(\mathbf{Y}_t) \rangle + 0$ (analytic result) in (19), performs better than the conventional scheme without variance reduction. Moreover, we plot the control process, representing the stochastic noise, in brown for which we analytically obtain $\langle \mathbf{Y}_t \otimes \mathbf{F}(\mathbf{Y}_t) \rangle = 0$ and which is subtracted from the blue solid line. Note however that the noise in \mathbf{Q}_t is not necessarily reduced for an equilibrium control variate in flow fields where \mathbf{Q}_t differs strongly from the equilibrium distribution, see also Bonvin and Picasso [17].

4. Results and discussion

In this section, we consider three different flow problems to illustrate the quality of our numerical implementation.

- First, we investigate the benchmark problem of a two-dimensional unsteady Poiseuille flow in a planar channel for the Oldroyd-B model and, in a further simulation, for the Hookean dumbbell model. As this problem has an analytical solution, we can state the computational discretization error.
- Second, we compare the FENE model with its FENE-P closure approximation for a two-dimensional 4 : 1 contraction flow problem. This problem has been analyzed in the literature and we use these results to validate our implementation.
- Third, we simulate a three-dimensional flow through a square-square contraction. As an analytical solution is not available, we compare our simulations with experimental measurements.

In general, we have applied an equilibrium control variate for all stochastic simulations. Furthermore, we often plot velocity and stress tensor results in combination with a zoomed picture (e.g. in Fig. 4). In this case, the zoomed region is indicated with a red rectangle in the full figure.

4.1. Unsteady Poiseuille flow of a Hookean dumbbell fluid

4.1.1. Problem specification

An unsteady Poiseuille flow in a planar channel results from a suddenly occurring constant pressure gradient in the channel direction (cf. Fig. 2). For a Hookean dumbbell fluid, this is one of the few transient viscoelastic problems that possesses an analytical solution for the velocity $u(y, t)$ and the stress tensor field $\boldsymbol{\tau}_p(y, t)$. In this case, both fields solely depend on the vertical position y and on time t .

The reference solution for the time-dependent velocity field is stated in Waters and King [38] as

$$\begin{aligned} u(y, t) &= U_{\max} \left[4y(1-y) \right. \\ &\quad \left. - 32 \sum_{n=1}^{\infty} \frac{\sin(Ny)}{N^3} \exp\left(-\frac{\alpha_N t}{2El}\right) G_N(t) \right] \end{aligned} \quad (20)$$

where $N = (2n - 1)\pi$, $y \in [0, 1]$, $t \geq 0$, and

$$G_N(t) = \cosh\left(\frac{\beta_N t}{2El}\right) + \frac{\gamma_N}{\beta_N} \sinh\left(\frac{\beta_N t}{2El}\right)$$

for $\beta_N^2 \geq 0$ with

$$\begin{aligned} El = \frac{De}{Re}, \quad \alpha_N = 1 + \beta El N^2, \quad \beta_N^2 = \alpha_N^2 - 4N^2 El, \\ \gamma_N = 1 + N^2 El(\beta - 2), \quad \beta_N = \sqrt{\beta_N^2}. \end{aligned}$$

For $\beta_N^2 < 0$, we set $\beta_N = \sqrt{-\beta_N^2}$ and $G_N(t)$ changes to

$$G_N(t) = \cos\left(\frac{\beta_N t}{2El}\right) + \frac{\gamma_N}{\beta_N} \sin\left(\frac{\beta_N t}{2El}\right).$$

As the second term in (20) decays to 0 for $t \rightarrow \infty$, the viscoelastic flow recovers the parabolic profile of the Newtonian solution.

Carew et al. [39] found analytical expressions for the stress components. The non-zero shear stress component is

$$\begin{aligned} \tau_{xy}(y, t) = \frac{1 - \beta}{El} \left[4(1 - 2y)El \right. \\ \left. - 32 \sum_{n=1}^{\infty} \frac{\cos(Ny)}{N^2} H_N(t) \right] + C_{xy}(y) \exp\left(-\frac{t}{El}\right) \end{aligned} \quad (21)$$

where $N = (2n - 1)\pi$ and $H_N(t)$ is related to $G_N(t)$ by

$$H_N(t) = \left(\frac{\beta}{N} - \frac{\alpha_N}{2ElN^3} \right) G_N(t) + \frac{1}{N^3} \frac{dG_N(t)}{dt}$$

and $C_{xy}(y)$ is a time-independent constant to ensure that $\tau_{xy}(y, t=0)=0$. Using (20) and (21) we numerically obtain the other non-zero stress tensor component τ_{xx} as

$$\tau_{xx}(y, t) = 2 \exp\left(-\frac{t}{El}\right) \int_0^t \tau_{xy}(y, s) \frac{\partial u}{\partial y}(y, s) \exp\left(\frac{t}{El}\right) ds. \quad (22)$$

We assume no-slip boundary conditions at the channel wall. This leads to a shear flow close to the wall boundary. Furthermore, the transient velocity component $u(t)$ and both stress components $\tau_{xx}(t)$ and $\tau_{xy}(t)$ exhibit over- and undershoots during the evolution towards a steady state. The fluid elasticity depends on the size of De . For $De = 1.0$, all components show several damped over- and undershoots. By increasing the Deborah number beyond $De = 1.0$, the first velocity overshoot is also increased but all other over- and undershoots in $u(t)$, $\tau_{xx}(t)$ and $\tau_{xy}(t)$ are damped out. We therefore concentrate on $De = 1.0$ to determine the accuracy of the unknowns although the multiscale approach allows using higher Deborah numbers.

As mentioned in the beginning of this section, we subdivide the convergence study for this benchmark problem in two subproblems:

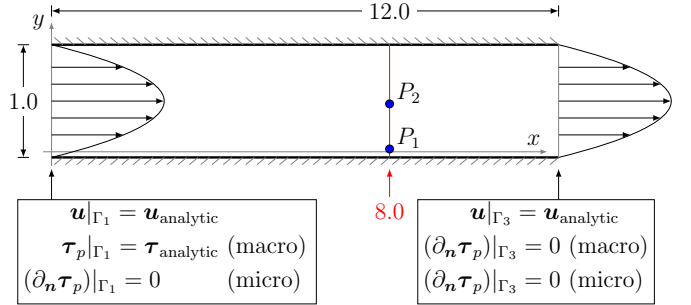


Figure 2: Poiseuille flow in a planar channel. We perform measurements on the line $x = 8.0$ or at the grid points $P_1 = (8.0, 0.075)$ and $P_2 = (8.0, 0.475)$.

- A convergence study of the Oldroyd-B model to the analytical solution and
- a stochastic convergence of the Hookean dumbbell to the Oldroyd-B model for a moderate and fixed mesh width to restrict computing time. In this case, we only increase the number of sample particles.

For both studies, we employ a channel of length 12.0 in the x-direction, of height 1.0 in the y-direction and of width 0.4 in the z-direction (cf. Fig. 2). As NaSt3DGPF solves the three-dimensional Navier-Stokes equations, we impose periodic boundary conditions in the z-direction to emulate the two-dimensional geometry. Moreover, we use $Re = 1.0$ and employ $\beta = 0.1$ for the viscosity ratio.

4.1.2. Convergence study for Oldroyd-B model

For the convergence study, we prescribe the analytical solution (20) of the velocity component u at the inflow and outflow boundary. On the channel walls, we set no-slip boundary conditions. Furthermore, we use the reference solutions (21) and (22) for the stress tensor on the inflow boundary and homogeneous Neumann boundary conditions (i. e. $(\partial_n \tau_p)|_{\Gamma_3} = 0$) on the outflow boundary. All initial values in the flow domain are zero.

Since all unknowns solely depend on y , any deviation in the flow domain from the inflow conditions is caused by a numerical error. Thus, we probe the flow on the line $x = 8.0$ over the full channel height, i. e. at $(8.0, y, 0.25)$ with $y \in [0, 1]$, and examine the solution of five consecutively x/y -refined meshes. Table 2 lists the number of grid cells and the corresponding mesh width for each level l . As the solution is constant in the z -direction, we keep the mesh width of 0.1 in this direction and measure all unknowns at $z = 0.25$ in the center of the second grid cell. For a more compact notation, we henceforth skip the third index in z -direction in all grid point descriptions.

For the error measurement, we employ the discrete L_l^2 -

Table 2: Mesh characteristics on different levels l used for the Oldroyd-B convergence study.

l	$\Delta x_l, \Delta y_l$	Δz_l	Cells/direction	Total cells
1	1.0×10^{-1}	0.1	$120 \times 10 \times 4$	4,800
2	5.0×10^{-2}	0.1	$240 \times 20 \times 4$	19,200
3	2.5×10^{-2}	0.1	$480 \times 40 \times 4$	76,800
4	1.25×10^{-2}	0.1	$960 \times 80 \times 4$	307,200
5	6.25×10^{-3}	0.1	$1920 \times 160 \times 4$	1,228,800

norm of an unknown f_l , i. e.

$$E_l(f_l) = \|f_{\text{analytic}} - f_l\|_{L^2_l} \\ \simeq \left(\sum_j |f_{\text{analytic}}(y_j) - f_l(y_j)|^2 \Delta y_l \right)^{\frac{1}{2}} \quad (23)$$

where $f_l(y_j)$ is a component of the numerical solution of either \mathbf{u} or $\boldsymbol{\tau}_p$ at position $(8.0, y_j)$ on mesh level l . Analogously, $f_{\text{analytic}}(y_j)$ denotes the reference solutions (20) - (22) evaluated at this position. Using these error values, we can compute the order of convergence p_l as

$$p_l = \frac{\log(E_l(f_l)/E_{l+1}(f_{l+1}))}{\log(2)}. \quad (24)$$

In Fig. 3 we show the error of the velocity component u for the first velocity overshoot at $t \approx 0.528$, for the first velocity undershoot at $t \approx 1.582$ and the error close to the steady state at $t = 10.0$. For a better illustration of the specified points in time, Fig. 8 shows the temporal evolution of u at grid point $P_2 = (8.0, 0.475)$. As expected, the error decreases with finer mesh widths. Additionally, Fig. 3 shows the errors for τ_{xx} and τ_{xy} , respectively.

We give the order of convergence for the plots of Fig. 3 in Table 3. For the horizontal velocity u we obtain a rate of second order in the over- and undershoot cases and at steady state, which is to be expected due to the combination of 2nd-order central differences and the 5th-order WENO scheme.

Obviously, the velocity overshoot situation is the more difficult one of the transient flow problem as the error on the finest mesh width is larger there. Nevertheless, the accuracy of u is very high, compared to the stress components τ_{xx} and τ_{xy} , for all mesh levels l . We illustrate this for the velocity overshoot along the y -axis in Fig. 4 for the three grid levels $l = 1, 3, 5$. Note that the top picture in Fig. 4 only shows the coarsest grid solution to maintain the visibility of the reference solution. Even though the error is largest at the overshoot point, we detect only minor deviations from the analytical solution. Here, the error in u is about 10^{-4} to 10^{-5} which is two orders of magnitude smaller than the error in $\boldsymbol{\tau}_p$.

The numerical error in $\boldsymbol{\tau}_p$ behaves differently for its components. Fig. 3 shows that the error in τ_{xy} is about one order of magnitude smaller than the error in τ_{xx} . This could be caused by the dependency of the time-discrete

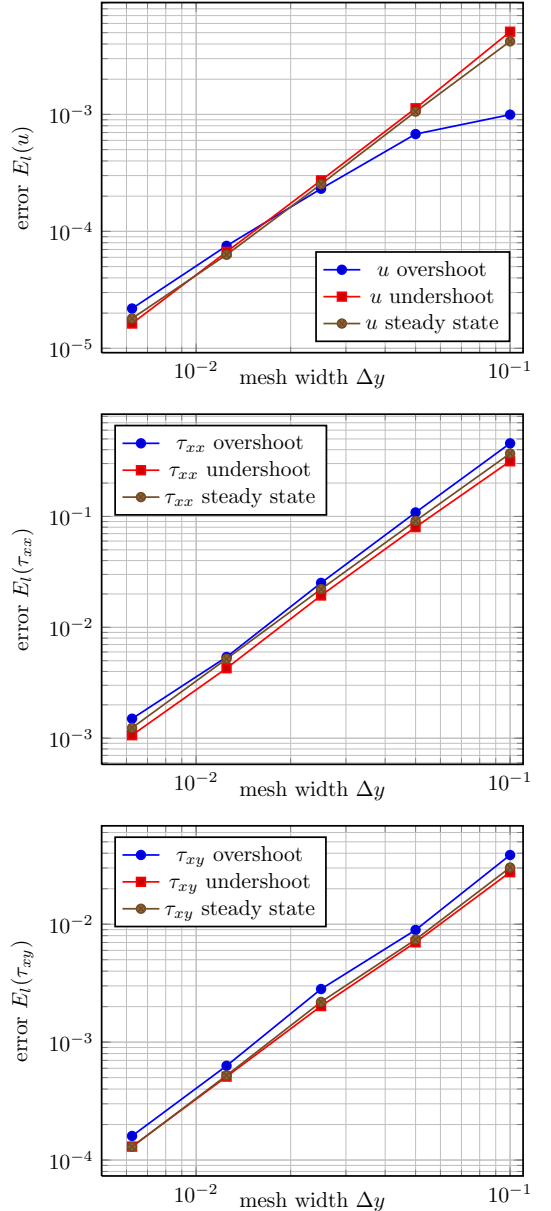


Figure 3: Top: convergence of u at $t \approx 0.528$ (overshoot), at $t \approx 1.582$ (undershoot) and at $t = 10.0$ (close to steady state). Middle: error reduction in τ_{xx} at $t \approx 1.194$ (overshoot), at $t \approx 2.17$ (undershoot) and at steady state. Bottom: error reduction in τ_{xy} at $t \approx 1.056$ (overshoot), at $t \approx 2.109$ (undershoot) and at steady state.

$\tau_{xy}^{(n+1)}$ on the velocity gradient only whereas, for the considered flow problem, $\tau_{xx}^{(n+1)}$ also depends on the previous time-step stress component $\tau_{xy}^{(n)}$ (insert $\mathbf{u} = (u, 0, 0)$ into the discretized Oldroyd-B equation (3)). Consequently, the error in τ_{xx} is larger than the error in τ_{xy} as it contains an additional error term. We obtain a convergence rate of order two.

In Fig. 5 we present the error in τ_{xx} for the stress overshoot case at $t \approx 1.194$ along the y -axis. We only plot τ_{xx} since it dominates the error in $\boldsymbol{\tau}_p$ and since the error at the

Table 3: Order of convergence for u , τ_{xx} and τ_{xy} at three different positions in time.

	overshoot			undershoot			steady state		
	u	τ_{xx}	τ_{xy}	u	τ_{xx}	τ_{xy}	u	τ_{xx}	τ_{xy}
time t	0.53	1.19	1.06	1.58	2.17	2.11	> 10	> 10	> 10
order									
p_1	0.55	2.07	2.11	2.17	1.98	1.98	1.99	2.02	2.03
p_2	1.56	2.11	1.67	2.05	2.05	1.80	2.07	2.04	1.76
p_3	1.62	2.22	2.16	2.03	2.18	1.99	2.00	2.09	2.07
p_4	1.78	1.85	1.98	2.03	2.00	1.97	1.81	2.07	2.01

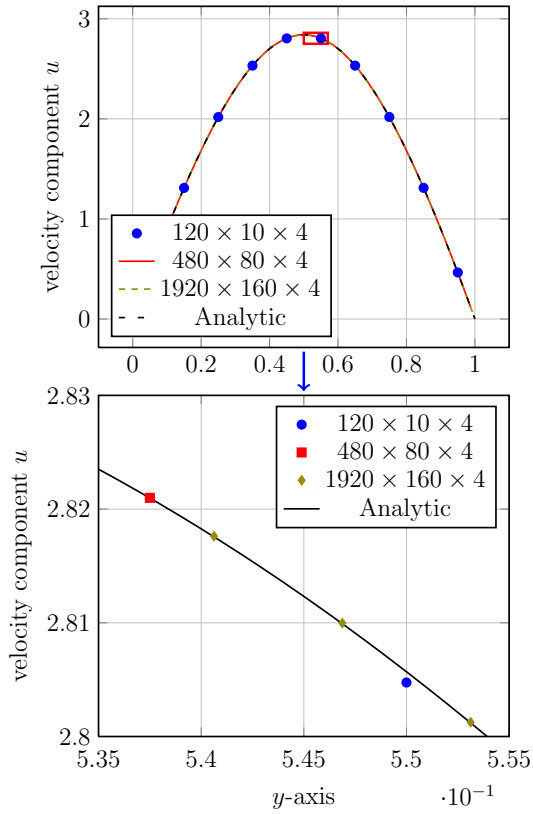


Figure 4: Velocity component u on the vertical channel wall during the velocity overshoot at $t \approx 0.528$.

stress overshoot exceeds the other errors anyway, as illustrated in Fig. 3. Again, we only detect minor deviations from the analytical solution. Altogether, this shows that our scheme accurately approximates the transient flow not only for the steady state but also for the previous over- and undershoot cases.

4.1.3. Stochastic convergence of the Hooke model to the Oldroyd-B model

In this subsection, we illustrate the convergence with probability one of the Hookean dumbbell to the Oldroyd-B model as stated by the law of large numbers. Using this approach, we obtain an error estimation for the other stochastic models such as the FENE dumbbell model (10). As the stochastic approach is much more demanding with

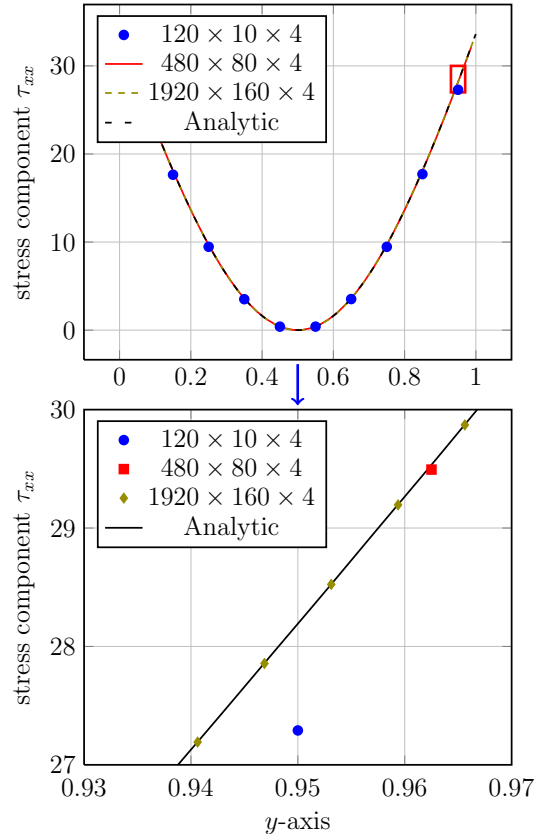


Figure 5: Stress component τ_{xx} on the y -axis during the stress overshoot at $t \approx 1.194$.

respect to the requirements on memory and computing time, we perform the simulations only on the grid $l = 2$ from Table 2. We cannot expect to yield better results for the Hookean dumbbell model than for the corresponding noise-free macroscopic model. Moreover, we expect an additional error for the multiscale approach caused by stochastic noise in the solution. To this end, we analyze the convergence to the Oldroyd-B model for fixed mesh width with an increasing number of Brownian configuration fields. Again, we use $Re = 1.0$, $De = 1.0$ and $\beta = 0.1$ for all simulations.

Fig. 6 compares the first normal stress component τ_{xx} for five simulations at position $P_1 = (8.0, 0.075)$ which is close to the channel's wall where the stresses reach their

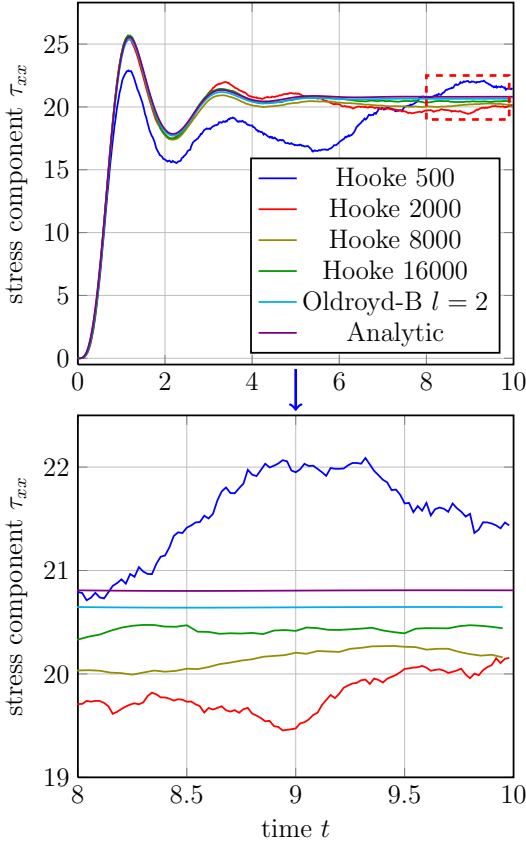


Figure 6: Temporal evolution of τ_{xx} at point $P_1 = (8.0, 0.075)$.

maxima. The first stress overshoot and the first undershoot are accurately resolved in all simulations with the exception of the coarsest simulation with $N_{BCF} = 500$. The simulation with $N_{BCF} = 500$ underestimates τ_{xx} until at about $t \approx 8.0$ the reference solution reaches a steady state. The more complex stochastic simulations with $N_{BCF} = 2000$, $N_{BCF} = 8000$ and $N_{BCF} = 16000$ better resolve the stress tensor over- and undershoots. Close to the steady state (cf. bottom picture in Fig. 6), the simulation with $N_{BCF} = 16000$ performs best with respect to the Oldroyd-B solution.

Fig. 7 displays the shear stress component τ_{xy} for the four stochastic simulations, that of the Oldroyd-B result and that of the analytical solution. The first stress overshoot is accurately resolved by the simulations $N_{BCF} = 2000$, 8000 and 16000 . However, only $N_{BCF} = 16000$ yields a high agreement for the second overshoot (cf. bottom picture in Fig. 7). For time integration, we used the explicit Euler-Maruyama method described in Section 3.2 with a constant time-step size of 10^{-4} which is much smaller than required from the respective CFL condition. Note that the usage of a constant and compliant time-step width for all stochastic simulations allows to investigate the effect of different sampling numbers N_{BCF} . Consequently, the dominant error in $\boldsymbol{\tau}_p$ results from the sample point error only. At steady state, the final values of τ_{xy} are compara-

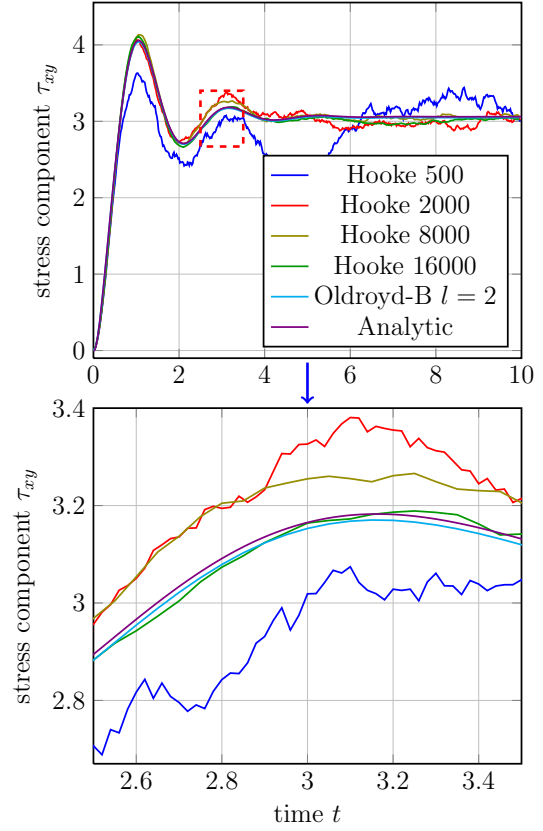


Figure 7: Evolution of stress component τ_{xy} at point $P_1 = (8.0, 0.075)$ over time.

ble in accuracy with the τ_{xx} results.

As our multiscale simulations at steady state exhibit a stochastic noise, we do not give a final value of $\boldsymbol{\tau}_p$ but an arithmetic mean over a time interval. To this end, we compute the expectation of $\boldsymbol{\tau}_p$ at $P_1 = (8.0, 0.075)$ as

$$\langle \boldsymbol{\tau}_p \rangle = \frac{1}{\#M} \sum_{t_i \in M} \boldsymbol{\tau}_p(t_i, P_1) \quad \text{for } M \equiv \{t_i \mid t_i \geq 8.0\} \quad (25)$$

with t_i randomly chosen. For the stochastic simulations we see that $\boldsymbol{\tau}_p$ is stationary after $t = 8.0$ since the analytical solution subsequently shows only minor changes which are below the stochastic error. For example, the analytical solutions for the annotated grid point are $\tau_{xx} \approx 20.80839$ and $\tau_{xy} \approx 3.06004$ at $t = 8.0$ and $\tau_{xx} \approx 20.80835$ and $\tau_{xy} \approx 3.06005$ at $t = 10.0$, respectively. Furthermore, we compute the variance of $\boldsymbol{\tau}_p$ at $P_1 = (8.0, 0.075)$ by using the formula

$$\sigma^2(\boldsymbol{\tau}_p) = \frac{1}{\#M} \sum_{t_i \in M} (\boldsymbol{\tau}_p(t_i, P_1) - \langle \boldsymbol{\tau}_p \rangle)^2 \quad (26)$$

separately for each stress tensor component with $M \equiv \{t_i \mid t_i \geq 8.0\}$.

In Table 4, we show the results for $\langle \boldsymbol{\tau}_p \rangle$, the variance $\sigma^2(\boldsymbol{\tau}_p)$ and the relative error in comparison to the analytical solution for different numbers of stochastic realizations

Table 4: Expectation of τ_{xx} and τ_{xy} at $P_1 = (8.0, 0.075)$, their relative error compared to the analytical solution and the variance for all stochastic simulations. For comparison, we state the Oldroyd-B and the analytical solution at $t = 10.0$.

N_{BCF}	$\langle \tau_{xx} \rangle$	$\varepsilon_{\text{rel}}(\tau_{xx})$	$\sigma^2(\tau_{xx})$	$\langle \tau_{xy} \rangle$	$\varepsilon_{\text{rel}}(\tau_{xy})$	$\sigma^2(\tau_{xy})$
500	21.5610	0.0362	0.409	3.2544	0.0635	0.177
2000	19.8004	0.0484	0.129	2.9927	0.0220	0.071
8000	20.1474	0.0318	0.038	3.0606	0.0002	0.021
16000	20.4310	0.0181	0.022	3.0238	0.0119	0.015
Oldroyd-B	20.6466	0.0077	0	3.0482	0.0039	0
Analytical	20.8084	0	0	3.0601	0	0

N_{BCF} . In general, the error in $\langle \tau_p \rangle$ does not monotonically decay because of the stochastic behavior. Due to Monte Carlo integration, the error in $\langle \tau_p \rangle$ is of the order $\mathcal{O}(N_{BCF}^{-1/2})$ whereas the variance decreases linearly in N_{BCF} .

In Fig. 8 we examine the velocity field at position $P_2 = (8.0, 0.475)$ close to the channel center over time. In comparison to the stress tensor components, we note that u is smooth even for the coarsely resolved stochastic simulation with $N_{BCF} = 500$. Although τ_p strongly oscillates in the flow domain for $N_{BCF} = 500$ (cf. Fig. 6 and Fig. 7 at $P_1 = (8.0, 0.075)$) this affects the velocity field only slightly. There is even a further increase in the smoothness of u for a larger number of stochastic samples which is visible in the zoom in Fig. 8 (bottom). The smoothness results from applying the same Wiener process for all N_g grid cells. On the other hand, we note that using more sample particles and thus increasing the accuracy in τ_p does not noticeably increase the accuracy in u for the considered range of particle numbers. The relative error in u at $P_2 = (8.0, 0.475)$ and $t = 10.0$ is $\varepsilon_{\text{rel}}(u) = 0.0014$ for the Oldroyd-B model with $l = 2$ and about $\varepsilon_{\text{rel}}(u) \approx 0.003$ for all stochastic levels. This shows that the error in τ_p dominates the error in u not only for $N_{BCF} = 500$ but also for $N_{BCF} = 16000$.

Similar to Fig. 4 in Section 4.1.2, we now compare the velocity over the full channel height at a fixed point in time. Fig. 9 displays the velocity profile at steady state and gives a zoom around the two center grid points. The error in u is already comparatively small for $N_{BCF} = 500$ and decreases only slightly for the higher resolved multiscale simulations. Using the discrete error norm of (23), we obtain a relative steady state error of $E_2(u) = 0.0029$ for $N_{BCF} = 500$ and of $E_2(u) = 0.0028$ for $N_{BCF} = 16000$ along the channel height. We expect an increase in the accuracy of u when the errors of u and τ_p are in the same order of magnitude and τ_p is no longer the dominant error term. Only then, an increase in the number of configuration fields, which decreases the error in the stress tensor, also decreases the error in u .

As a result, we conclude the following for the specified benchmark experiment:

1. A multiscale approach with stochastic samples decreases the accuracy of the velocity field u compared

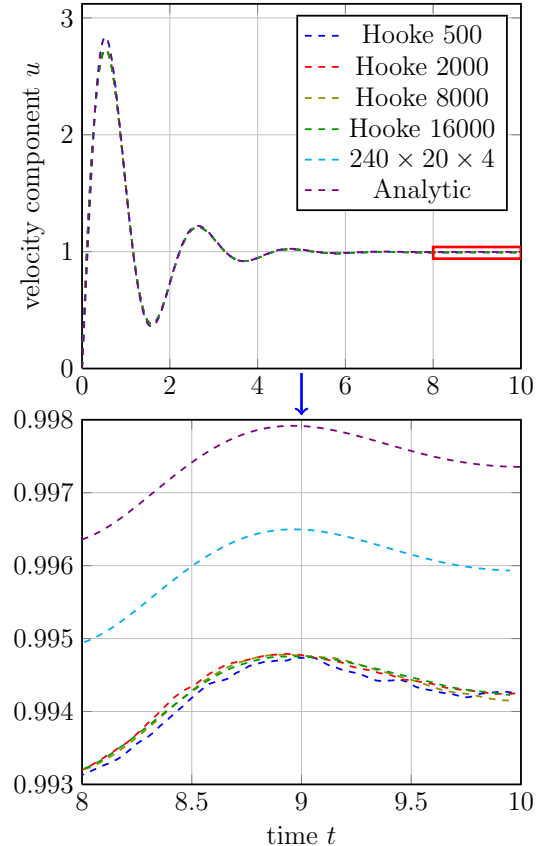


Figure 8: Horizontal velocity u over time at $P_2 = (8.0, 0.475)$.

to a macroscopic approach. This reduction in accuracy is however much smaller in size than one would expect from the stochastic behavior of τ_p only.

2. The velocity field remains smooth and does not adopt the oscillating behavior of τ_p .
3. Multiscale simulations with the annotated number of grid cells and configuration fields deliver velocity fields with an accuracy that is adequate for comparisons with experimental results (i.e. the relative error in u is about 0.3%).

This also applies to the FENE model in Section 4.2 and Section 4.3.

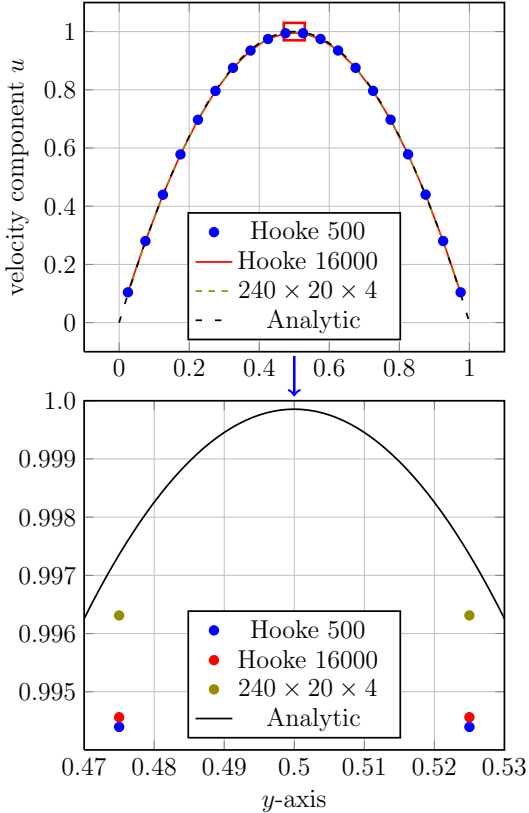


Figure 9: Steady state velocity profile of u in y -direction.

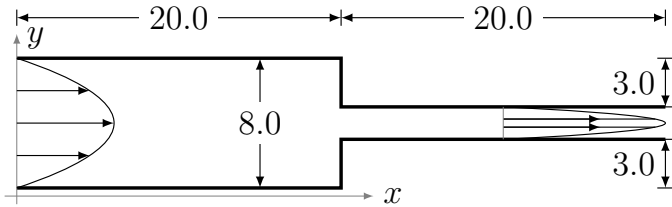


Figure 10: Two-dimensional contraction flow geometry.

4.2. FENE flow in a planar 4:1 contraction

4.2.1. Problem specification and parameter setting

In the second benchmark problem, we focus on the differences between the FENE dumbbell model and its FENE-P closure approximation. For this purpose, we investigate a planar flow in a 4:1 contraction according to Wapperom et al. [40] to allow for comparisons. Although the problem is restricted to two dimensions, it is closely related to the three-dimensional problem in Section 4.3 as the flow field in both problems has a singularity at the contraction.

In Fig. 10 we depict the flow geometry. We decide for half of the downstream's channel height as characteristic length scale L_c and set $L_c = 1.0$. The length both of the upstream and downstream channel is chosen as 20.0. In accordance with Wapperom et al. [40] we use $\rho = 0.098$, $\eta_s = 0.05$, $\eta_p = 0.65$, $\lambda = 0.6$ and $\beta = \eta_s/(\eta_s + \eta_p) = 1/14$ for the fluid. On the upper

Table 5: Mesh characteristics on different levels l used for the FENE and FENE-P simulations.

l	$\Delta x_l, \Delta y_l$	Δz_l	Cells/direction	Total cells
1	0.5	0.5	$80 \times 16 \times 3$	3,840
2	0.25	0.5	$160 \times 32 \times 3$	15,360
3	0.125	0.5	$320 \times 64 \times 3$	61,440
4	0.0625	0.5	$640 \times 128 \times 3$	245,760

and lower channel walls we employ no-slip boundary conditions. Analogously to the unsteady Poiseuille flow in Section 4.1 we prescribe a parabolic velocity profile at the inflow boundary but in this case we assume the profile to be fully developed already. Using $U_c = 23/3$ as average velocity at the outflow boundary and the definitions in (7), we obtain a Reynolds number $Re \approx 1.07$ and a Deborah number $De = 4.6$. Furthermore, we use $b = 10$ for the extensibility parameter in the FENE and FENE-P model.

In Table 5 we list the different mesh levels l that are used in the simulations. Again we use periodic boundary conditions in the z -direction to emulate a two-dimensional geometry. On the finest mesh $l = 4$ we employ 32 grid cells to resolve the downstream's channel height. Furthermore, we use $N_{BCF} = 4000$ for each simulation. Note here that, for reasons of comparability, we use the FENE-P model in its multiscale formulation.

For temporal discretization we employ the semi-implicit 2nd-order Crank-Nicolson scheme. In contrast to the convergence study in Section 4.1, we now use the largest available time-step that fulfills the CFL condition for the convective velocity terms. The time steps for the simulations are of order $\mathcal{O}(10^{-2})$ for $l = 1$ and of order $\mathcal{O}(10^{-3})$ for $l = 4$.

4.2.2. 2D simulation results

First, we compare the results for the FENE and the FENE-P model on the finest mesh $l = 4$ analogously to Wapperom et al. [40]. We then concentrate on the FENE model and investigate the convergence behavior by comparing different levels $l = 1, 2, 3, 4$. At last, we consider the meshes $l = 3$ and $l = 4$ for the FENE-P model.

In Fig. 11 and Fig. 12 we illustrate the evolution of the lower corner vortex for the FENE and for the FENE-P model computed on mesh width $l = 4$. Note that the visualized time points in both figures are chosen such that they coincide with the streamline visualizations in Fig. 15 and Fig. 20 in Wapperom et al. [40] to allow for comparison. In both simulations a corner vortex develops and starts to increase in size at the beginning. The corner vortices reach their maximum size at about $t \approx 0.35$ when a lip vortex at the re-entrant corner forms. The evolution then differs between the FENE and FENE-P model. The two vortex regions for the FENE model attach at $t \approx 0.7$ but can still be distinguished. The vortex intensity increases up to $t \approx 3.0$ when a steady state is reached in which two separated vortex regions exist. The FENE-P model predicts

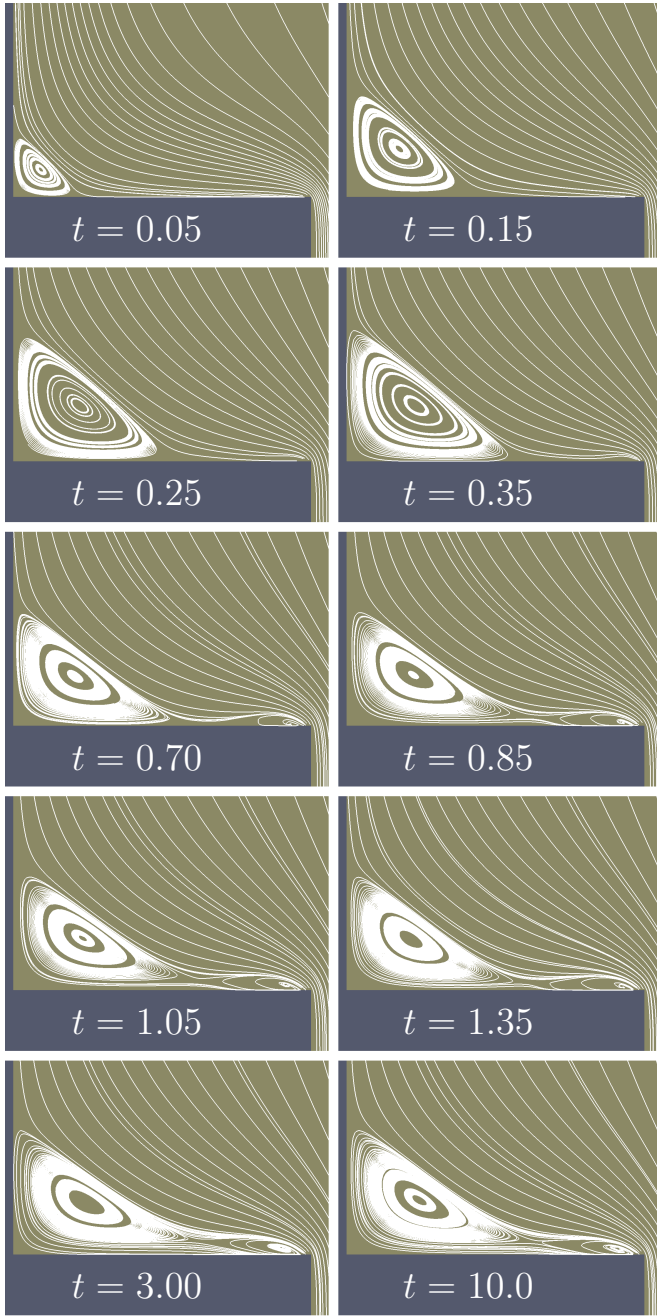


Figure 11: Corner vortex evolution for the FENE model.

a lip vortex that is larger in size and is still distinct from the corner vortex till about $t \approx 0.85$. The vortices then attach and form a structure that also consists of two separated vortex cores. Compared to the FENE model, the lip vortex is larger in its size but the size of the corner vortex is slightly reduced. The vortices further increase up to $t \approx 3.0$ when the system reaches a steady state. Comparing the steady state results, i.e. a vortex structure that is dominated by the corner vortex in the FENE model on the one hand and a vortex structure with a more pronounced lip vortex in the FENE-P model on the other hand, shows that the FENE-P model deviates from the FENE model

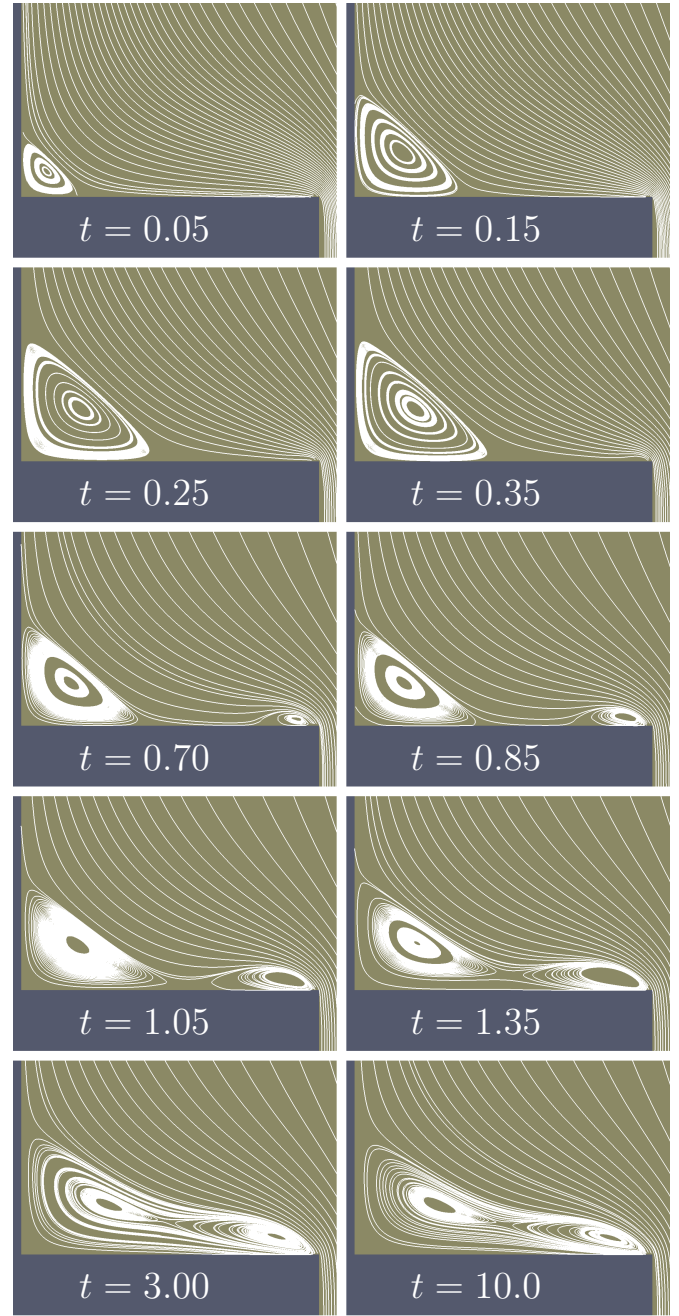


Figure 12: Corner vortex evolution for the FENE-P model.

for this contraction flow problem.

Compared to the literature, our FENE simulation results show an excellent agreement with the results in Wapperom et al. [40]. On the other hand, our results for the FENE-P model differ from the literature at the final stage of the simulation. The two predicted vortices in [40] merge at $t \approx 1.35$ and form one large lip vortex in contrast to the two separated vortex cores that we show in Fig. 12. We further discuss these differences for the FENE-P model, depending on the mesh width l , at the final part of this section.

In Fig. 13 to Fig. 15 we display the steady state FENE

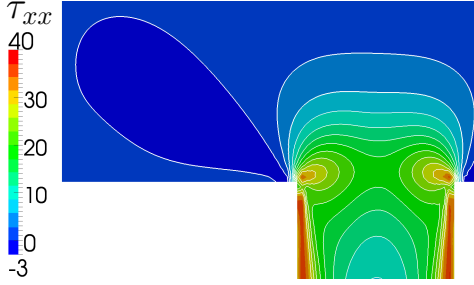


Figure 13: FENE contour lines of stress component τ_{xx} .

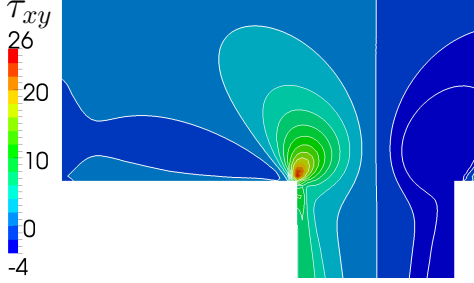


Figure 14: FENE contour lines of stress component τ_{xy} .

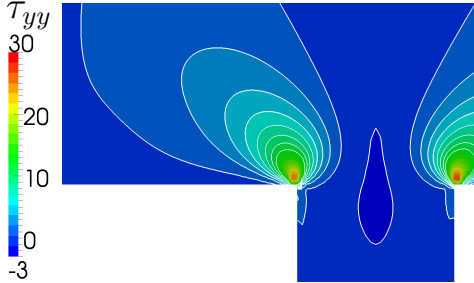
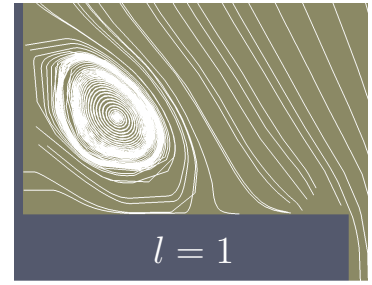


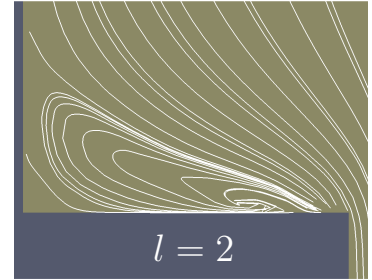
Figure 15: FENE contour lines of stress component τ_{yy} .

stress components τ_{xx} , τ_{xy} and τ_{yy} at $t = 10.0$. Although the absolute stress tensor profiles are symmetric at the channel's centerline, the figures show both corner singularities. Hence, it is viable to analyze the symmetry of the numerical solution. The stochastic BCFs only show minor oscillations and small deviations from the symmetry. The perspective in all figures was chosen such that it matches Fig. 19 in Wapperom et al. [40]. For a better comparison, we scaled τ_{xy} in Fig. 14 such that the isolines are adapted to the lower part of the channel. All stress components have their maximum value at the contraction corner. The shape of the stress components closely resembles the results in [40]. There, higher stress tensor values at the singularity were obtained as their adaptive mesh geometry resolves the corner singularity better but, apart from the singularity point, the agreement of the absolute values is high. The singularity would be better resolved on the next finer mesh level $l = 5$. But altogether, this leads to only minor differences in the corner vortex structure in Fig. 11.

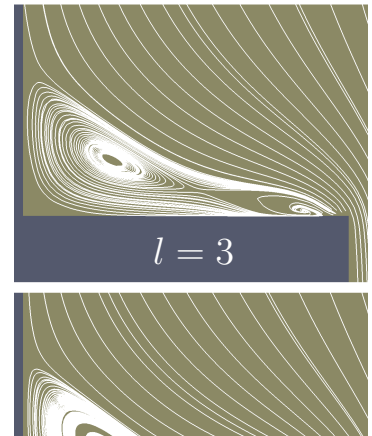
In Fig. 16 we compare the steady state FENE vortex



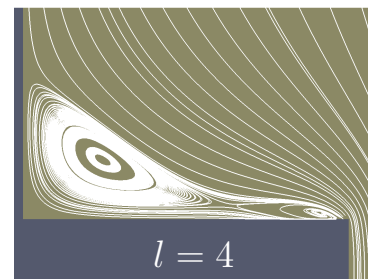
$l = 1$



$l = 2$



$l = 3$



$l = 4$

Figure 16: Corner vortex at $t = 10.0$ using the FENE model on different mesh widths l .

structure for different mesh widths l as listed in Table 5. One large salient corner vortex occurs on the coarsest mesh level $l = 1$ but a lip vortex as in Fig. 11 is not yet resolved. On mesh level $l = 2$, the shape of the vortex resembles the steady state result in Fig. 11 but the grid still resolves one large vortex only. Finally, a separate lip and corner vortex develop for $l = 3$ and $l = 4$. The results on both meshes show only minor differences. We therefore conclude that the results at $l = 4$ are close to a converged solution. Furthermore, all important vortex characteristics are already resolved on $l = 3$.

The situation differs for the FENE-P model. In Fig. 17 we depict the medium and final stage of the simulation for $l = 3$ and for $l = 4$. Up to $t \approx 0.85$ there is no difference in the vortex evolution. At $t \approx 0.85$ both vortices attach for $l = 3$ on the one hand but are still distinct for $l = 4$ on the

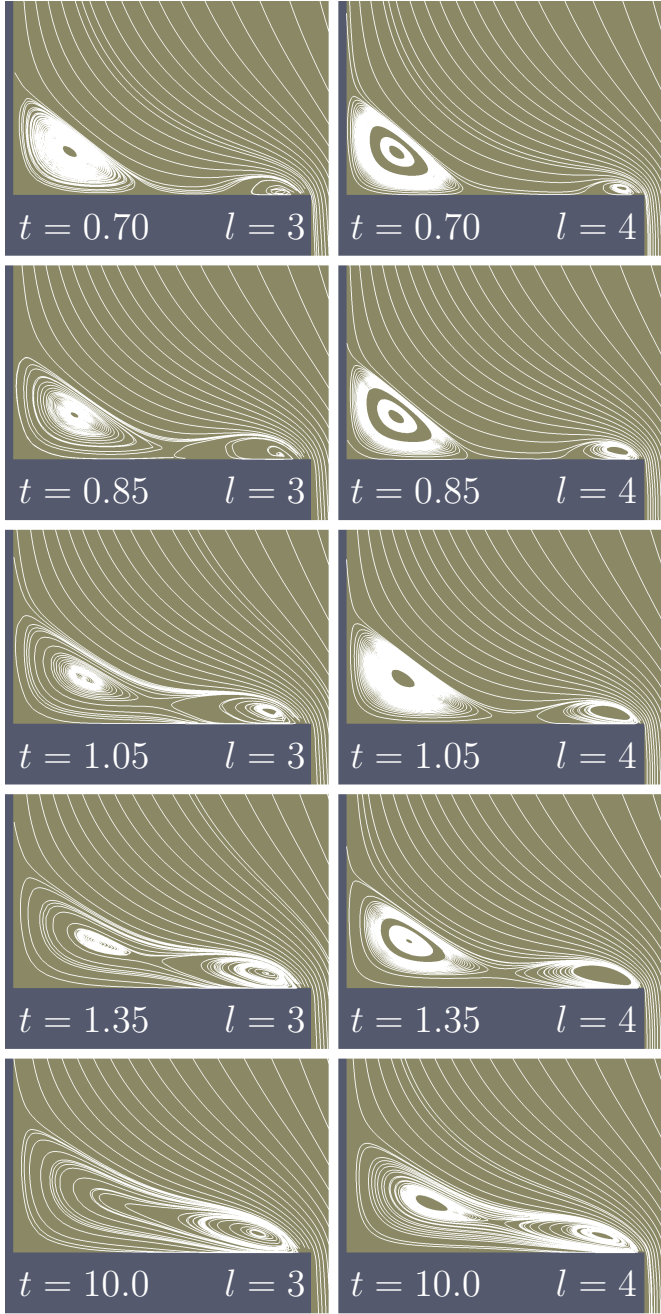


Figure 17: Differences in the finale stage of the simulation for the FENE-P model depending on the mesh width l .

other hand. For $l = 4$ this vortex attachment occurs later at about $t \approx 1.05$. At $t \approx 1.35$ the corner vortex for $l = 3$ combines with the lip vortex and forms one large vortex structure. As mentioned before, for $l = 4$ both vortices can still be separated up to the steady state. We assume that the mesh on level $l = 3$ is not sufficiently fine to show the corner vortex at steady state. Interestingly, the edge of the complete vortex structure is similar for both meshes. We also note that our results at $l = 3$ closely resemble the results in Wapperom et al. [40]. As the mesh in this article is finest resolved at the singularity point apart from the

corner vortex, it might be possible that simulations in [40] on a refined mesh also display two steady state vortices for the FENE-P model.

In the following Section 4.3 we use a mesh for the simulation of a three-dimensional square-square contraction that is similar in its x - y -resolution to the mesh width $l = 3$ in Table 5. Although the mesh was sufficiently fine to show all relevant flow phenomena for the FENE model in the considered two-dimensional case, this was different for the FENE-P results. On the other hand, the high Deborah number flows that occur in Section 4.3 lead to a corner vortex that is much larger in size than the filigree vortex structure in this section, cf. vortex sizes in Fig. 11 and Fig. 23. We therefore assume that it is sufficient to perform the computationally demanding three-dimensional simulations on a mesh with the chosen accuracy.

4.3. FENE fluid flow in a three-dimensional square-square contraction

4.3.1. Modeling and parameter setting

Now we compare the results of our simulations for a shear-thinning fluid in a square-square contraction with that of laboratory experiments. For this purpose, we use the measurements of Sousa et al. [41] for a non-Newtonian solution composed of 40.0% (w/w) glycerol, 59.9% (w/w) water and polyacrylic acid (PAA) with a weight concentration of 600 ppm for comparison. This experiment extends previous findings from Sousa et al. [42] for a Newtonian and a Boger fluid to shear-thinning fluids.

The flow geometry consists of a quadratic upstream channel with side length $2H_1 = 24$ mm which contracts into a smaller downstream channel with side length $2H_2 = 6$ mm (i. e. contraction ratio 4:1). The upstream channel's length is 82.5 mm; the length of the downstream channel is 15 mm which results in a total domain size of 97.5 mm \times 24 mm \times 24 mm. We discretize this domain with a finite difference grid that consists of $N_g = 260 \times 64 \times 64$ grid cells, i.e. with an equidistant mesh width $h = 0.375$ mm. We use double precision machine numbers for each of the three BCF components. Thus, the total memory requirement is approximately 19 GB. For illustration, we show the corresponding computational grid in Fig. 18 and a 2D cut of the contraction region in Fig. 19. The 2D cut also shows that the downstream channel's height is resolved with 16 grid cells.

Our simulation parameters for the shear-thinning fluid correspond to those used by Sousa et al. [41]. There, the authors employ a simplified Phan-Thien Tanner model (SPTT). They give the parameters for their fluid fit as $\epsilon = 0.06$ for the extensibility parameter, $\eta_p = 1.62$ Pa s for the zero polymer shear viscosity, $\eta_s = 0.03$ Pa s for the solvent shear viscosity, and $\lambda = 32$ s for the fluid's relaxation time, respectively. Using these values in (7), we derive a viscosity ratio $\beta = 0.0182$ for the momentum equation (4) and for Kramers' relation (12). We use $L_c = H_2 = 3$ mm as characteristic length scale in (7) and obtain, with average

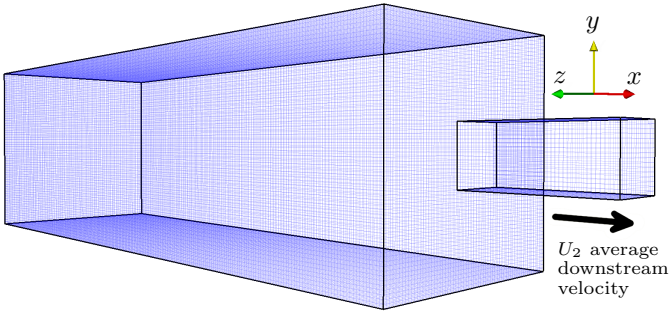


Figure 18: Visualization of the 3D mesh for the contraction flow problem.

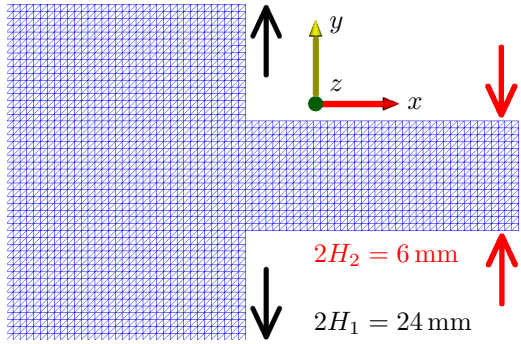


Figure 19: A zoomed 2D cut of the contraction region.

downstream velocities $U_c = U_2 = 2.26 \text{ mm/s}$, 10.1 mm/s and 14.2 mm/s , the Deborah numbers $De_2 = 24.1, 108$ and 157 . This definition leads to Reynolds numbers below 1 . Consequently, elasticity is more important than inertia at higher flow rates.

At a sufficient distance from the contraction region, the velocity profile for a shear-thinning fluid shows only minor deviations from a Newtonian profile in a square-square channel. For this reason, we prescribe the analytical solution for a constant viscosity fluid on the inflow domain as boundary condition, compare e.g. White [43]. In this case, the ratio from the value at the centerline to the average velocity is ≈ 2.0963 .

The Hookean dumbbell model (9) used in the benchmark experiment does not predict shear-thinning and is not applicable to the experimental fluid. On the other hand, the FENE dumbbell model (10) predicts shear-thinning reasonably well. It contains an extensibility parameter b to match the fluid's shear thinning behavior. This extensibility parameter is related to the extensibility parameter ϵ in the SPTT model but, as both models do not coincide, b has to be determined empirically. For this purpose, we compare the shear-dependent behavior of the SPTT fit by Sousa et al. [41] with different choices for b in the FENE model. Herrchen and Öttinger [26] considered various FENE dumbbell and closure models using the values $b = 20, 50, 100$. They interpret the parameter b roughly as the number of monomer units, which form the polymer that is represented by the dumbbell. The authors

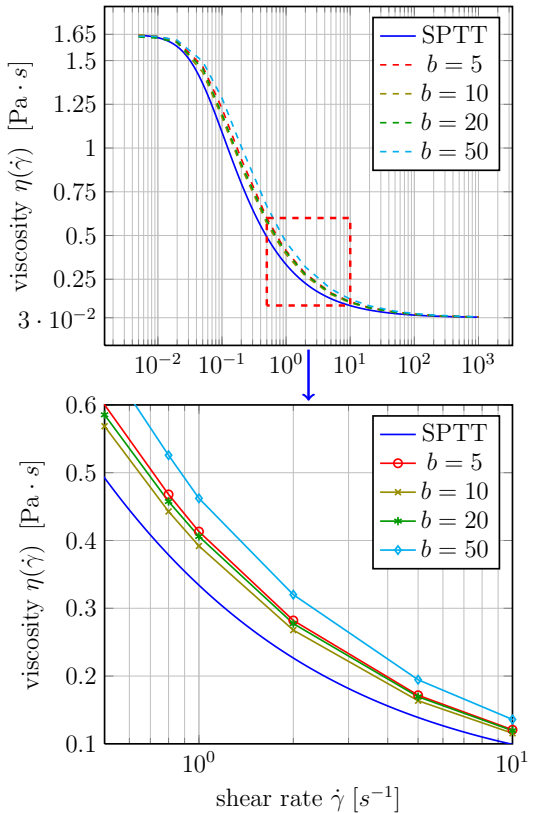


Figure 20: Apparent viscosity over shear rate $\dot{\gamma}$ for the SPTT and the 3D FENE dumbbell models with $b = 5, 10, 20, 50$.

suggest to use values in the range $b \in [20, 100]$ since lower values do not result in a physical model any more and larger values are closely related to the Oldroyd-B model.

In Fig. 20 we investigate the shear-rate dependent viscosity function. The apparent viscosity matches $\eta(\dot{\gamma}) = \eta_s + \eta_p = 1.65 \text{ Pa s}$ in the limit of zero shear and matches $\eta(\dot{\gamma}) = \eta_s = 0.03 \text{ Pa s}$ for large values of $\dot{\gamma}$ due to shear-thinning effects. Relevant shear rates $\dot{\gamma}$ for the contraction flow are of the order $\dot{\gamma} \approx U_2/H_2 = 0.75 \text{ s}^{-1}$ at $De_2 = 24.1$ and of the order $\dot{\gamma} \approx U_2/H_2 = 4.9 \text{ s}^{-1}$ at $De_2 = 157$. For this scope of application, we note that $b = 5, 10, 20, 50$ differ from the SPTT fit.

Another variable of interest is the first normal stress coefficient defined as $\Psi_1 = (\tau_{xx} - \tau_{yy})/\dot{\gamma}$. As illustrated in Fig. 21, the FENE model with $b = 20$ is in high agreement with the SPTT model fit for the relevant range of $\dot{\gamma}$. Consequently, we employ $b = 20$ for our multiscale FENE simulations. Since the fluid characterization in Sousa et al. [41] was performed to fit the fluid's shear behavior only, we can not directly infer that the fluid's extensional behavior is also characterized properly. For this reason, deviations might occur at the $2H_1$ -normalized channel's centerline $(x, 0.5, 0.5)$ as an extensional flow is predominant there.

The material functions in Fig. 20 and in Fig. 21 for the FENE dumbbell models were obtained from 25 steady

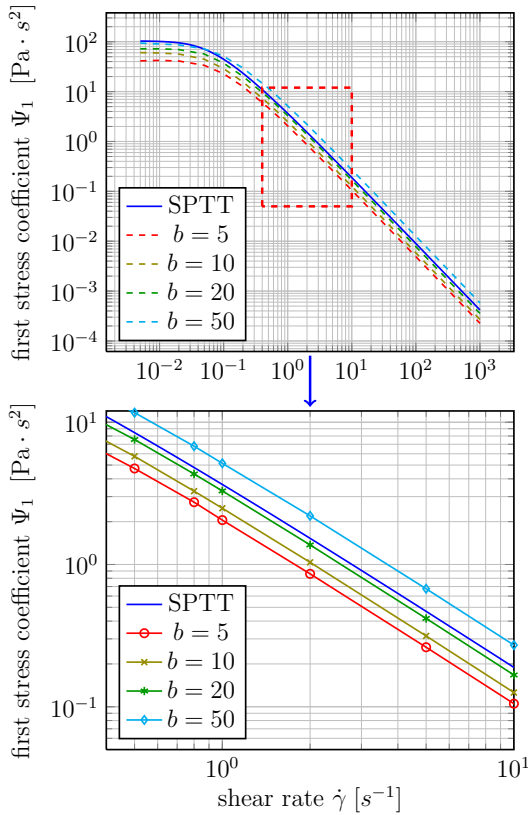


Figure 21: The first stress coefficient Ψ_1 over shear rate $\dot{\gamma}$ for different 3D FENE dumbbell models and the SPTT model.

shear flow simulations with $\dot{\gamma} \in [10^{-2} \text{ s}, 10^3 \text{ s}]$ and $N_g = 1$ for each of the values $b = 5, 10, 20, 50$. Each simulation evolved $N_{BCF} = 10^6$ sample particles for fixed $\dot{\gamma}$ until steady state was reached. Then, the resulting stresses were measured. The steady states stress tensor values finally delivered $\eta(\dot{\gamma})$ and $\Psi_1(\dot{\gamma})$ for the corresponding $\dot{\gamma}$.

We perform all contraction flow simulations with stochastic values of $N_{BCF} = 800$ samples per grid cell. Altogether, the total number of configuration fields is $800 \times 260 \times 64 \times 64 \approx 850 \cdot 10^6$. In contrast to the previous 2D Poiseuille flow simulations in Section 4.1, we do not artificially restrict the time-step width but use the largest possible time-step. The step size for the semi-implicit 2nd-order Crank-Nicolson scheme is primarily restricted by the CFL condition $\Delta_t \leq \Delta_x / |u_{\max}|$ since the horizontal velocity component u is dominant over the components v and w for the chosen flow direction. Due to the implicitness of the schemes with respect to the diffusion operator, there is no restriction for the diffusive velocity terms and for the stochastic PDE in case of the FENE spring force. The time step sizes are in the order of $\mathcal{O}(10^{-2} \text{ s})$ for $De_2 = 24.1$ and of order $\mathcal{O}(10^{-3} \text{ s})$ for $De_2 = 157$. Each simulation required 10-14 weeks on 64 CPUs of our parallel cluster *Siebengebirge* to reach a steady state. This emphasizes the huge computational requirements that are necessary

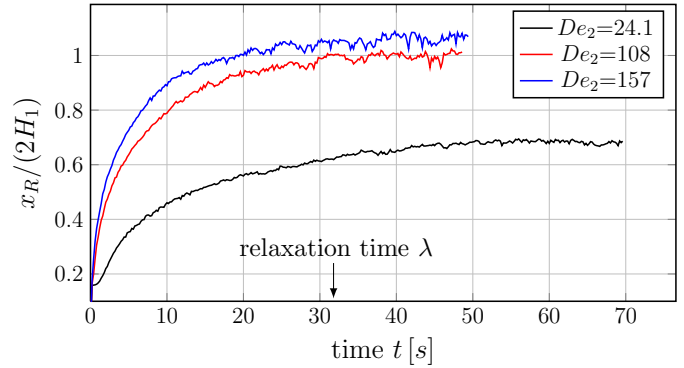


Figure 22: Plot of the $2H_1$ -normalized vortex lengths on the central plane $z = H_1$ over time.

for 3D multiscale simulations.

4.3.2. 3D simulation results

An important limiting factor is the numerical simulation time. Therefore, we have to recognize when the system has reached its steady state to avoid unnecessary calculations. The results by Sousa et al. [41] indicate that the system possesses a steady solution for Deborah numbers up to $De_2 \approx 300$.

To this end, we measure the vortex sizes over time on the plane $z = H_1$, compare Fig. 22, and terminate the computation when the vortex size or the reattachment length has reached a plateau. This results in a simulation time of $t \approx 70 \text{ s}$ for $De_2 = 24.1$ and of $t \approx 50 \text{ s}$ for $De_2 = 108$ and $De_2 = 157$, respectively. The size of the vortex length is determined by the extension of the horizontal velocities' zero contour, i. e. $\min\{x/(2H_1) | u(x, y, 0.5) = 0\}$ with u as the velocity component in flow direction. The plot of the vortex length over time shows some minor oscillations at steady state which occur due to the stochastic stress tensor treatment.

An increase of the flow rate, which also enhances elastic effects, leads to a strong vortex enlargement for the investigated shear-thinning fluid. This is in contrast to Newtonian fluids for which an increase in flow inertia, due to the absence of elastic effects, decreases the size of the upstream vortex. Fig. 23 shows the steady state flow field for all three multiscale simulations. The size of the upper vortex is indicated by a white dashed line. All vortices are convex-shaped which is in agreement to the results by Sousa et al. [41] for high flow rates. Furthermore, a solid white line gives a typical streamline. The streamline at $De_2 = 24.1$ runs parallel to the channel wall to the left side of the lower vortex and then moves inwards into the downstream channel. This behavior is typical for Newtonian flows. In contrast, the streamlines at $De_2 = 108$ and at $De_2 = 157$ diverge towards the channel walls shortly before they reach the vortex and then run inwards into the downstream channel. This effect is more pronounced at $De_2 = 157$ than at $De_2 = 108$ which is in agreement with the results by Sousa et al. [41].

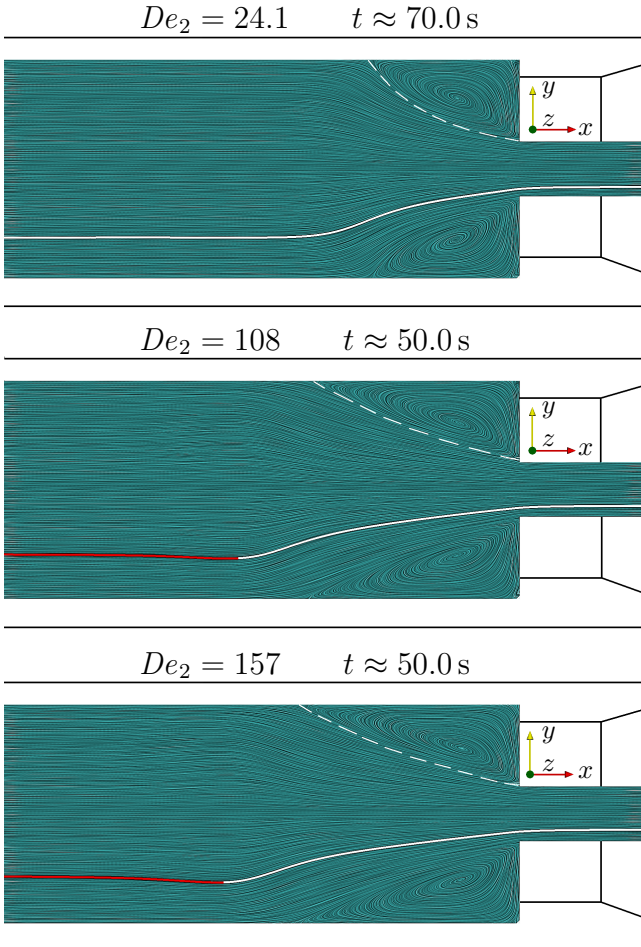


Figure 23: Simulation results at $De_2 = 24.1, 108$ and at $De_2 = 157$ at steady state on the central plane $z = H_1$. The phenomena of streamlines divergence, indicated in red on a typical streamline, occurs for the high Deborah number flows but not for $De_2 = 24.1$.

In Fig. 24 and Table 6 we compare the steady state vortex sizes obtained from our simulations with those of the experimental measurements obtained by Sousa et al. [41]. Our vortex length results at $De_2 = 24.1$ coincide very well with those of the experimental measurements. Additionally, we have performed further simulations for low Deborah numbers of order $\mathcal{O}(1)$ using a macroscopic PTT model. In this case, the vortices are smaller in size but still agree with the experimental measurements as shown in Fig. 24. For the macroscopic PTT simulations we employed the same model parameter $\epsilon = 0.06$ for the extensibility as used by Sousa et al. [41]. The low Deborah number flows for $De_2 = 0.5$ and $De_2 = 1.0$ simultaneously show a corner vortex and an additional lip vortex near the re-entrant corner, as illustrated in Fig. 25, where the vortex regions are indicated with white dashed lines. The additional lip vortex is not present for $De_2 = 2.0$. This coincides with general findings, for instance reported by Sousa et al. [42], namely that a coexistence of lip vortex

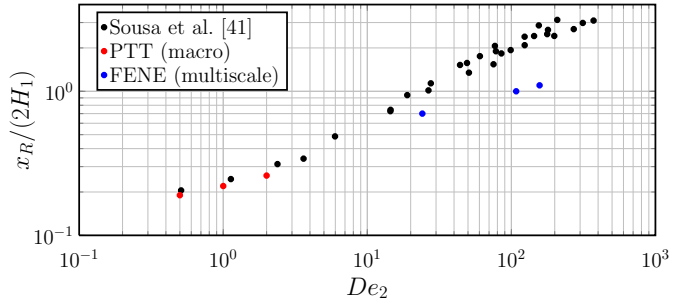


Figure 24: Comparison of the $2H_1$ -normalized vortex lengths on the central plane.

Table 6: Comparison between the experimental measurements by Sousa et al. [41] and our multiscale simulations for different Deborah numbers.

Deborah number De_2	24.1	108	157
Sousa et al. [41]	≈ 0.9	≈ 2.0	≈ 2.4
multiscale FENE	≈ 0.7	≈ 1.0	≈ 1.1

and corner vortex only occurs in a small transition regime where the fluid's elasticity becomes dominant. In contrast to the behavior at high flow rates, the vortices are slightly concave-shaped at $De_2 = 0.5$ and $De_2 = 1.0$. Due to the fluid's high relaxation time λ our macroscopic PTT simulations become unstable at $De_2 \approx 4$. Similar problems are common in literature for high Deborah number flows (cf. the high Weissenberg number problem analyzed in Keunings [44]). One reason for these stability issues stems from the large relaxation time of $\lambda = 32\text{s}$ for the experimental fluid.

The stability problem in macroscopic approaches can be partly avoided by rewriting the constitutive model in terms of the conformation tensor as proposed by Fattal and Kupferman [45]. This ansatz was used by Sousa et al. [41] to achieve numerically stable results with the PTT model for Deborah numbers of order $\mathcal{O}(10)$. Nevertheless, the authors state that their implementation is unstable at Deborah numbers 24.1 and higher for the investigated fluid so that a numerical analysis as in Fig. 23 was not possible. In contrast, the multiscale BCF method did not show any stability problems at the considered Deborah numbers which indicates its robustness. On the other hand, we observe that our implementation underestimates the experimental results by a factor of 2 at $De_2 = 108$ and at $De_2 = 157$, respectively. This discrepancy becomes the more pronounced the higher the flow elasticity is.

Furthermore, the numerically computed vortices are sensitive to various parameters, like e.g. the dumbbell's extension parameter b . To illustrate this, we show the vortex sizes at $De_2 = 157$ for different values of b on the central plane $z = H_1$. We plot the upper vortex at $t = 3\text{s}$ with $De_2 = 157$ for $b = 10, 20$ and 40 in the upper part of Fig. 26. Due to the high computational effort, these simulations were not computed to the steady state. Since

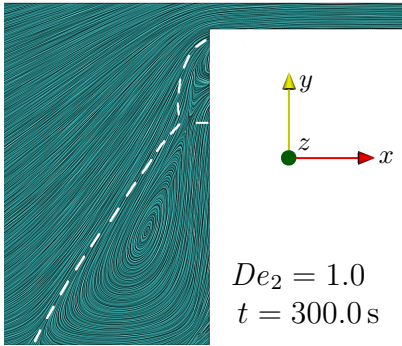
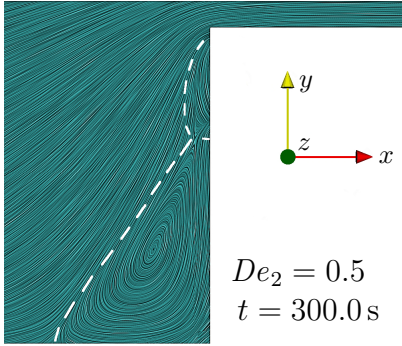


Figure 25: Coexistence between a lip and a concave-shaped corner vortex for a macroscopic PTT model for $De_2 = 0.5$ and for $De_2 = 1.0$.

the simulation time is $t = 3.0$ s, the vortices have not yet reached their full size. The normalized vortex sizes at this intermediate time point are $x_R/2H_1 \approx 0.58$ for $b = 10$, $x_R/2H_1 \approx 0.61$ for $b = 20$, and $x_R/2H_1 \approx 0.57$ for $b = 40$. Moreover, the vortices also differ in their shape. The zero contour of u is highlighted in Fig. 26 with a solid white line to clarify these differences. For $b = 40$ the zero contour of the horizontal velocity component u , indicated by a solid white line, has a more pronounced s-like shape as for $b = 10$ although the normalized vortex length is similar.

The differences are more pronounced in the FENE-P model for $b = 20$. We show the simulations results for this model in the lower part of Fig. 26. The normalized vortex size in this case is $x_R/2H_1 \approx 0.60$ which is similar to the FENE simulation result for $b = 20$. However, in contrast to the ellipsoidal vortex shape that occurs in the FENE simulations, the corner vortex in the FENE-P model has a more circular shape. For this reason, the area that is covered by the vortex in the FENE-P model is larger in size and the vortex core is shifted towards the channel's centerline. Comparable differences also occurred in Section 4.2 for a two-dimensional contraction flow.

In Fig. 27 and Fig. 28 we compare the axial velocity profiles on the centerline for $De_2 = 24.1$ and for $De_2 = 108$. Note that the horizontal axis is scaled with $2H_2$ and that its origin is shifted to the contraction. Again, we observe similar velocity profiles for $De_2 = 24.1$ and deviations for $De_2 = 108$. The deviations in the velocity profiles for $De_2 = 108$ are related to an underestimation

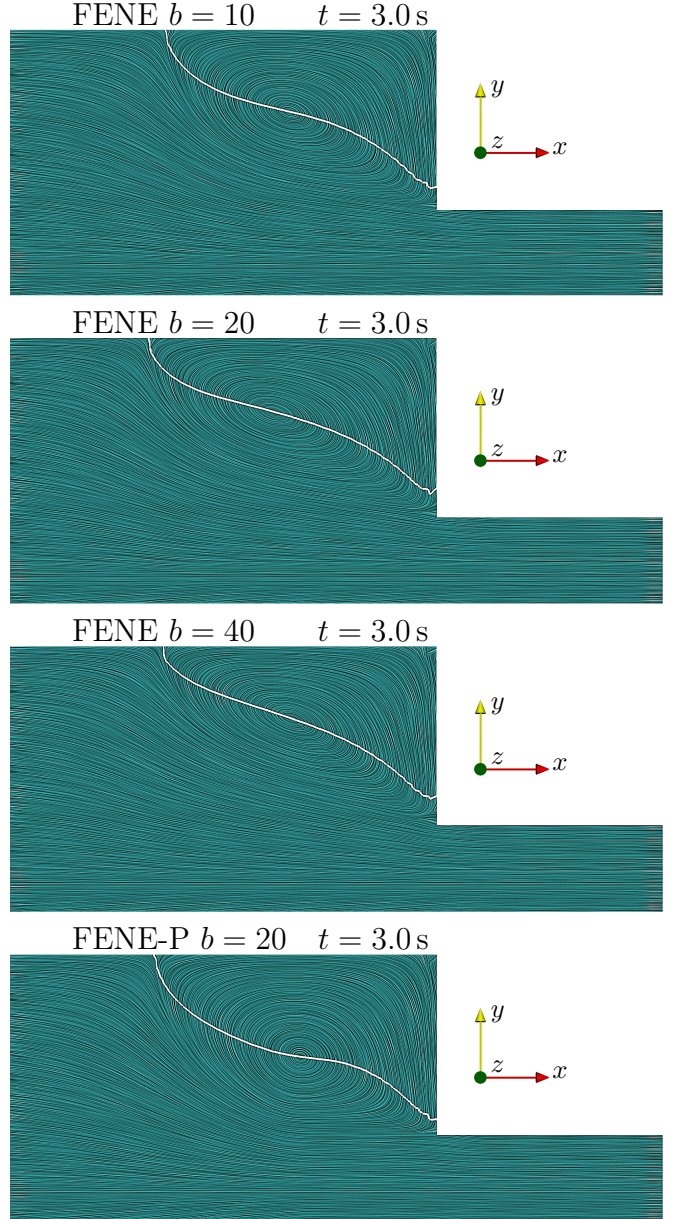


Figure 26: Comparison of the FENE model with the FENE-P model for different values of b at $De_2 = 157$.

of the vortex size. The fluid's acceleration in the simulations is delayed as the vortex size is smaller compared to the experiment findings. Apart from this, the starting point for the acceleration is shifted to the left in the experimental measurements and in the multiscale simulation compared to $De_2 = 24.1$ (cf. Fig. 27 and Fig. 28).

Another aspect in Fig. 28 are velocity under- and overshoots. First, the experiments by Sousa et al. [41] reveal an overshoot when the fluid enters the downstream channel. However, our simulations do not result in an overshoot at steady state. Since we are not aware of the experimental error sizes we cannot interpret these differences. Second, the authors mention an undershoot before the fluid starts

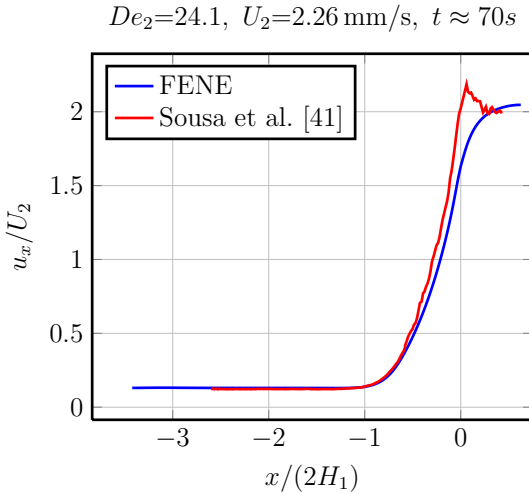


Figure 27: Axial velocity profiles on the channel centerline for $De_2 = 24.1$.

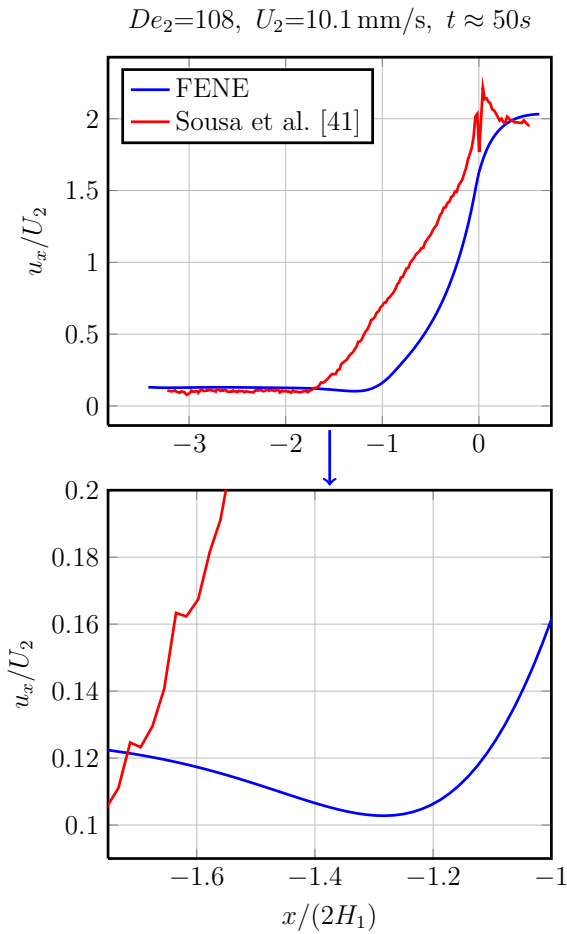


Figure 28: Axial velocity profiles on the channel centerline for $De_2 = 108$.

to accelerate which is more pronounced for the higher Deborah numbers. This undershoot also occurs in our simulations and is highlighted in the zoomed part in Fig. 28

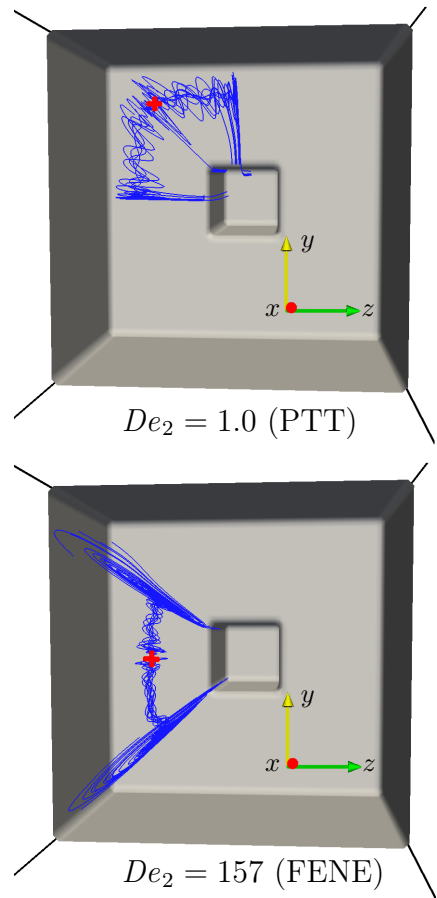


Figure 29: 3D vortex patterns for nearly Newtonian (top) and for high Deborah numbers flows (bottom).

(bottom). Interestingly, the undershoot seems to be more pronounced in the simulations than in the experimental measurements.

The square-square contraction flow geometry differs from axial or planar contraction geometries as it features 3D flow phenomena. In Fig. 29 we illustrate the 3D vortex structure. For nearly Newtonian flows (top), particles that enter the flow domain on a diagonal plane, such as $(y - H_1) + (z - H_1) = 0$, rotate by 45° towards one of the central planes $y = H_1$ or $z = H_1$, respectively. Note that the perspective in Fig. 29 coincides with the flow direction, i.e. x -direction, and that the upstream channel is clipped.

Literature findings often state an inversion of this 3D vortex pattern for highly elastic flows. This effect is also reported for Boger fluids which suggests that elasticity and not shear-thinning is responsible for the occurrence of flow inversion (cf. results by Sousa et al. [42] for Boger fluids). For high Deborah number flows, such as for $De_2 = 157$ in Fig. 29 (bottom), particles enter the flow domain on the planes $y = H_1$ or $z = H_1$, respectively, and rotate the other way around towards one of the diagonal planes before going through the contraction. Sousa et al. [41] estimate that the effect of flow reversal for the experimental fluid occurs for Deborah numbers larger than ≈ 1.5 . Referring

to our multiscale results, all three simulations show an inversion of the flow field streamlines.

A further variable of interest is the evolution of the pressure profile p on the centerline through the contraction. Due to the elasticity of the fluid, the measured pressure drop is not only caused by the pressure difference between the two Poiseuille flows in the upstream and downstream channel but results also from the extensional flow in the contraction. The increase in the pressure drop is usually investigated with the dimensionless Couette correction C defined as

$$C = \frac{\Delta p_{\text{total}} - |\frac{dp}{dx}|_{\text{fd,u}} \Delta x_u - |\frac{dp}{dx}|_{\text{fd,d}} \Delta x_d}{2\tau_w}. \quad (27)$$

Here, Δp_{total} is the total pressure drop at two specific locations in the upstream and downstream channel. These locations have been chosen such that the flow can obtain its fully developed Poiseuille profile at the points of measurement. Furthermore, $|\frac{dp}{dx}|_{\text{fd,u}}$ and $|\frac{dp}{dx}|_{\text{fd,d}}$ denote the pressure gradients at these two positions and Δx_u and Δx_d represent the distances to the midpoint of the contraction. τ_w in (27) denotes the average downstream wall shear stress. For a square-square channel, τ_w can be approximated by $|\frac{dp}{dx}|_{\text{fd,d}} H_2/2$.

In Fig. 30, we plot the dimensionless pressure gradient $(\nabla_{x/H_2} p)/((\eta_s + \eta_p)U_2/H_2)$ on the channel's centerline. The coordinate system in this plot has been shifted such that its origin indicates the beginning of the contraction. The pressure gradient is strongly affected in the interval $[-H_2, H_2]$ for all three multiscale flows. First, there is a small pressure recovery shortly before the contraction point which then leads to a strong pressure drop at $x/H_2 = 0$.

Fig. 31 shows the Couette correction C as a function of De_2 for both, the macroscopic and the multiscale simulations. We have chosen the positions for measuring the pressure profiles at $x/H_2 = -24$ and at $x/H_2 = 4.8$. Even though the pressure measurement point in the downstream channel is relatively close to the contraction point, Fig. 30 confirms that the pressure gradient is close to its fully developed value there.

In Fig. 31, a large extra pressure drop occurs for the higher Deborah number flows which increases with the flow rate. This extra pressure drop is related to the vortex enhancement in the upstream channel corner as illustrated in Fig. 23. Therefore, the FENE dumbbell model seems to be able to predict the large increase in the Couette correction which is measured for certain fluids in contraction flows. Note here that other viscoelastic models like Oldroyd-B are not able to predict such an increase in the Couette correction (cf. results by Alves et al. [46] for Boger fluids).

Koppol et al. [21] investigated the accuracy of a macroscopic FENE-P closure model, a multiscale FENE dumbbell and a multiscale three-bead-spring FENE model for the prediction of the extra pressure drop in a two-dimensional 4:1:4 contraction-expansion flow. The experimental fluid was a constant viscosity 0.025 wt % PS/PS Boger

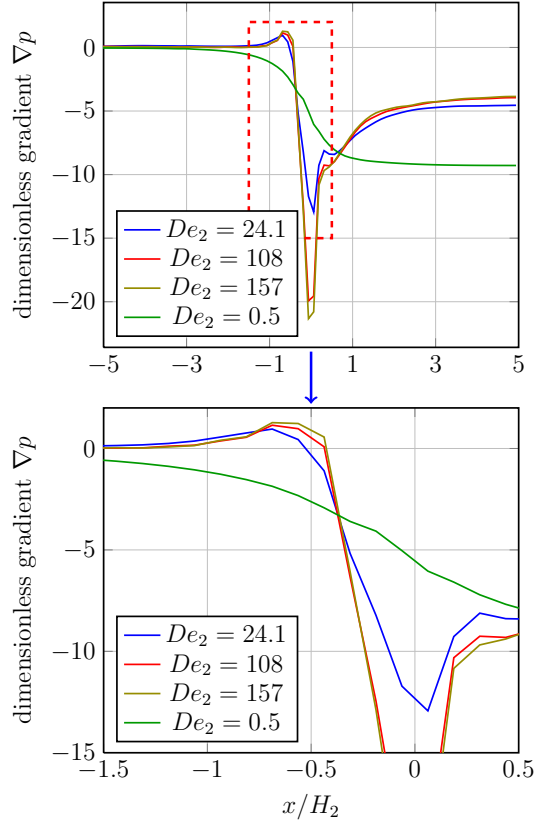


Figure 30: Pressure gradient measured over centerline.

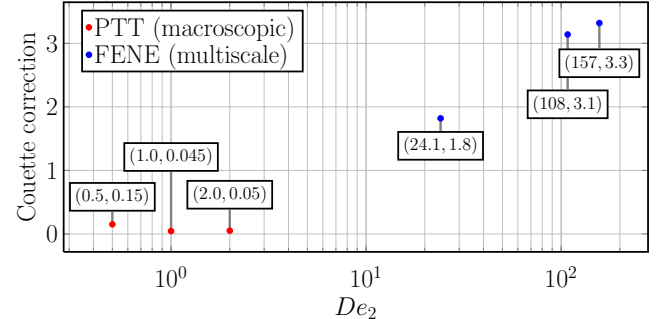


Figure 31: Couette correction for the SPTT and FENE dumbbell simulations.

fluid. In general, both multiscale FENE models were able to predict the large extra pressure drop enhancement. However, compared to the FENE dumbbell model, the authors emphasize the better agreement of the three-bead-spring FENE with the experimental data at higher Deborah numbers. Even though we investigate a different problem, we expect a comparable uncertainty in our absolute pressure drop values for the higher Deborah number flows in Fig. 31 similar to the results in Koppol et al. [21].

A multiscale approach delivers additional information, compared to classical macroscopic approaches, due to the actual description of the polymer configurations. In Fig. 32

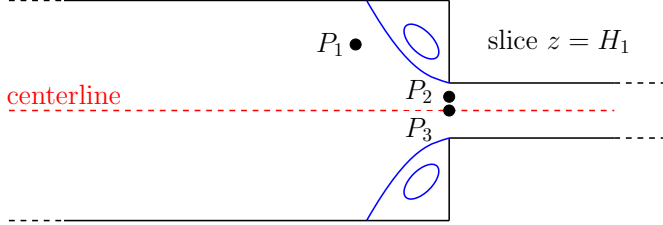


Figure 32: 2D cut of the channel geometry in which the positions P_1 , P_2 , and P_3 are indicated.

we indicate three different $2H_1$ -normalized positions

$$\begin{aligned}P_1 &= (-1.09375, 0.875, 0.5) \\P_2 &= (0, 0.59375, 0.5) \\P_3 &= (0, 0.5, 0.5)\end{aligned}$$

that are employed for the discrete configuration vectors $\mathbf{Q}_t^{(i)}$, $i = 1, \dots, 800$. Position P_1 and P_2 lie roughly on the same streamline so that they represent the same configuration at two different points in time, in the upstream area and in the point in time of contraction. Position P_3 directly lies on the channel centerline at the downstream channel's entrance. We analyze the polymeric orientations at the two different Deborah numbers $De_2 = 24.1$ and $De_2 = 157$, respectively. A similar analysis was performed by Prieto et al. [19] for a 2D planar contraction flow.

In Fig. 33 we give the polymer configurations at P_1 for two different Deborah numbers. We first visualize all three components of the configuration vectors $\mathbf{Q}_t^{(i)}$, $i = 1, \dots, 800$ (top). Then, we restrict the configuration vector to its first and second component Q_x and Q_y in the center, to clarify the actual shape of the 3D structure (center). At last we state the probability density function for the squared distance function \mathbf{Q}^2 which is limited by $b = 20$ (bottom). We obtain a typical shear flow pattern for both flows. Furthermore, the higher flow rate at $De_2 = 157$ leads to a stronger molecule extension as shown in the corresponding density function.

At position P_2 indicated in Fig. 34 most of the stochastic samples are elongated close to their maximum. This reflects the occurrence of strong tensions at the contraction corner. Nevertheless, the components on the xy -plane are still rotated against the horizontal axis as in Fig. 33. In contrast to this, the configurations at position P_3 on the centerline are aligned with the axis of the flow direction.

The sample particles in Fig. 35 have a similar distribution for both flows but the support is different. The vertical spread at $De_2 = 157$ in the y - and z -direction is strongly reduced compared to the flow at $De_2 = 24.1$. Since an extensional flow occurs at the centerline, the configuration fields are aligned with the flow and reach their maximum extension there.

Using the Brownian configuration fields in each grid cell, we compute the components of the polymeric stress tensor. In Fig. 36 we show the τ_{xx} component on a plane

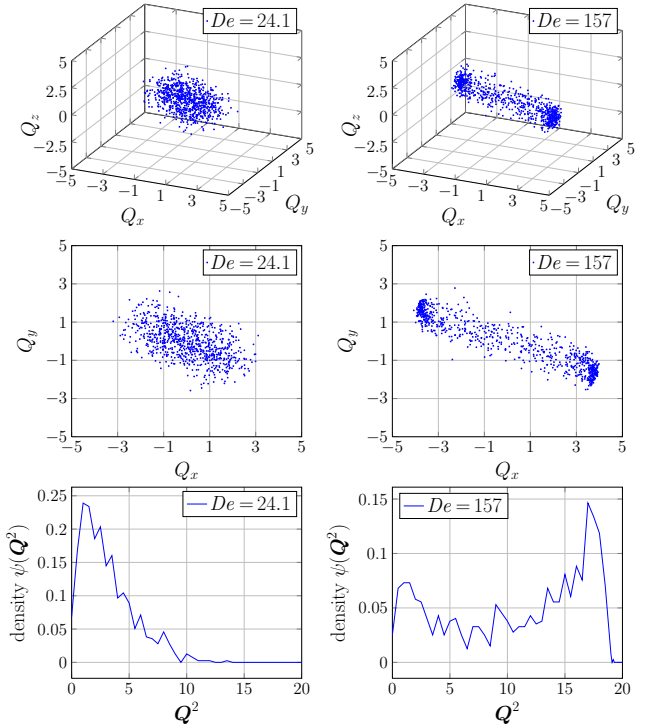


Figure 33: Shear flow behavior upstream of contraction (P_1) for two different Deborah numbers.

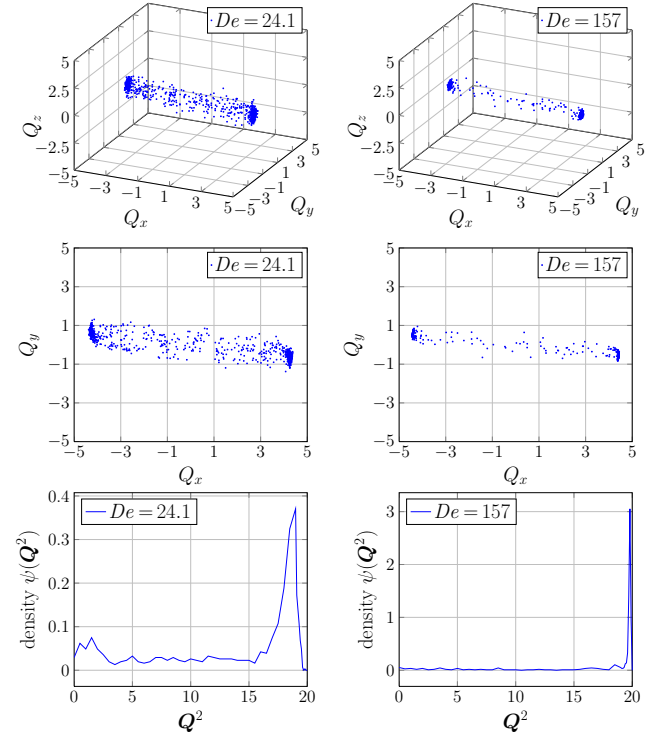


Figure 34: Polymer configuration at the re-entrant corner (P_2) for two different Deborah numbers.

at $De_2 = 157$. As reported by Keunings [5] for the BCF method, the stress field is smooth in space at a fixed

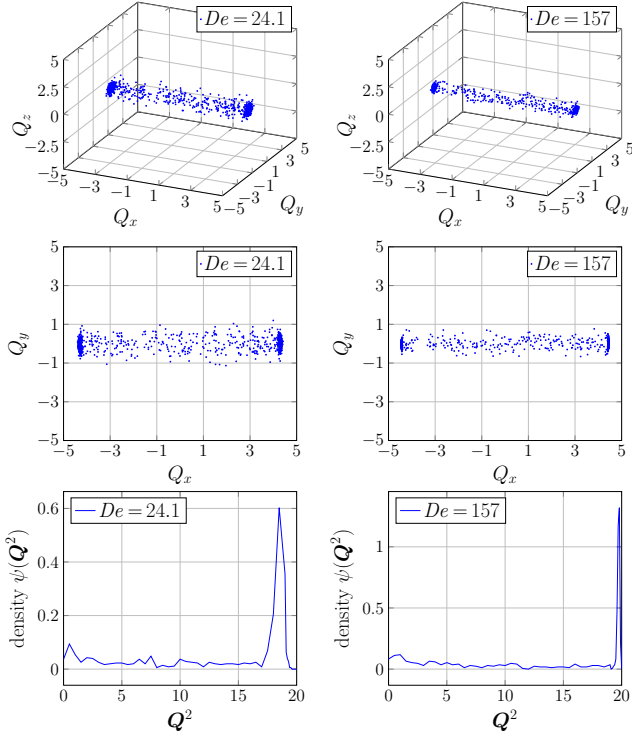


Figure 35: Extensional behavior at centerline (P_3) for two different Deborah numbers.

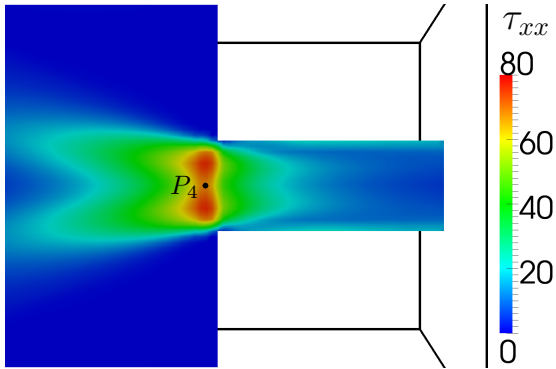


Figure 36: First normal stress component τ_{xx} on the slice $z = H_1$ at $t = 50$ s for $De_2 = 157$.

point in time. This is caused by the locally correlated Brownian force as described in Section 2.2. The stress component has two peaks close to the corner singularity that overlap on the centerline (cf. $2H_1$ -normalized position $P_4 = (-1/32, 0.5, 0.5)$ in Fig. 36). For the same Deborah number flow we give the τ_{xy} component in Fig. 37. In comparison to the results for τ_{xx} , the shear stress is smaller in size and takes its maximum at the corner singularity. As indicated before, τ_{xy} is smooth in space at a fixed point in time.

To analyze the stochastic behavior of the BCF method, we plot both stress components in Fig. 38 at two different positions over time. We show τ_{xx} at point $P_4 = (-1/32, 0.5, 0.5)$ on the centerline and τ_{xy} at point $P_5 = (-1/32, 0.390625, 0.5)$.

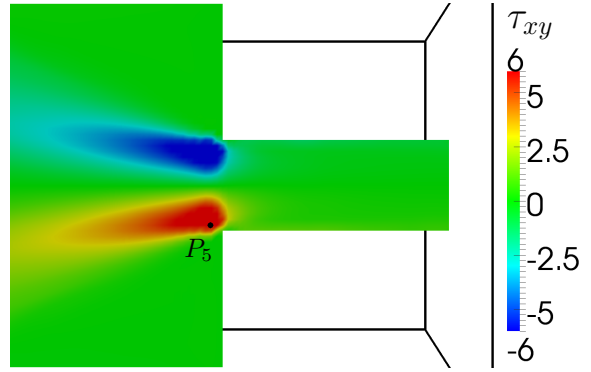


Figure 37: Shear stress component τ_{xy} on the slice $z = H_1$ at $t = 50$ s for $De_2 = 157$.

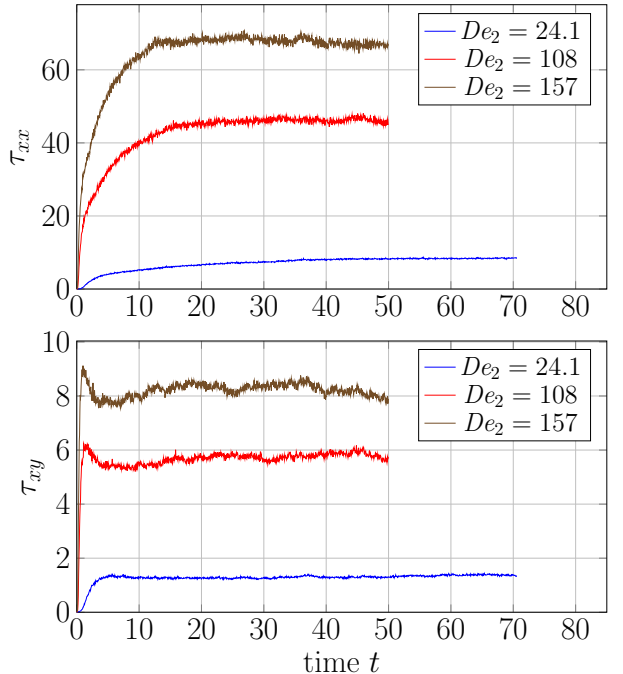


Figure 38: Plot of the stress component τ_{xx} at $P_4 = (-1/32, 0.5, 0.5)$ and of τ_{xy} at $P_5 = (-1/32, 0.390625, 0.5)$.

$0.390625, 0.5)$ close to the contraction corner. Both points are defined analogously to P_1, P_2 and P_3 and are indicated in Fig. 36 and Fig. 37, respectively. Depending on the Deborah number, the steady state stress values are different in their magnitude. For the higher flow rates we obtain larger shear and normal stresses. τ_{xx} increases monotonically over time until its steady state value is reached. On the other hand, τ_{xy} has a stress overshoot at the beginning and then decreases to its final value. The stress overshoot is more pronounced at $De_2 = 157$ than for the flows with lower elasticity. The oscillation in both components is caused by the stochastic approach and can be reduced by using more samples particles or by employing a more advanced variance reduction scheme.

In Fig. 39 we show the steady state stress components

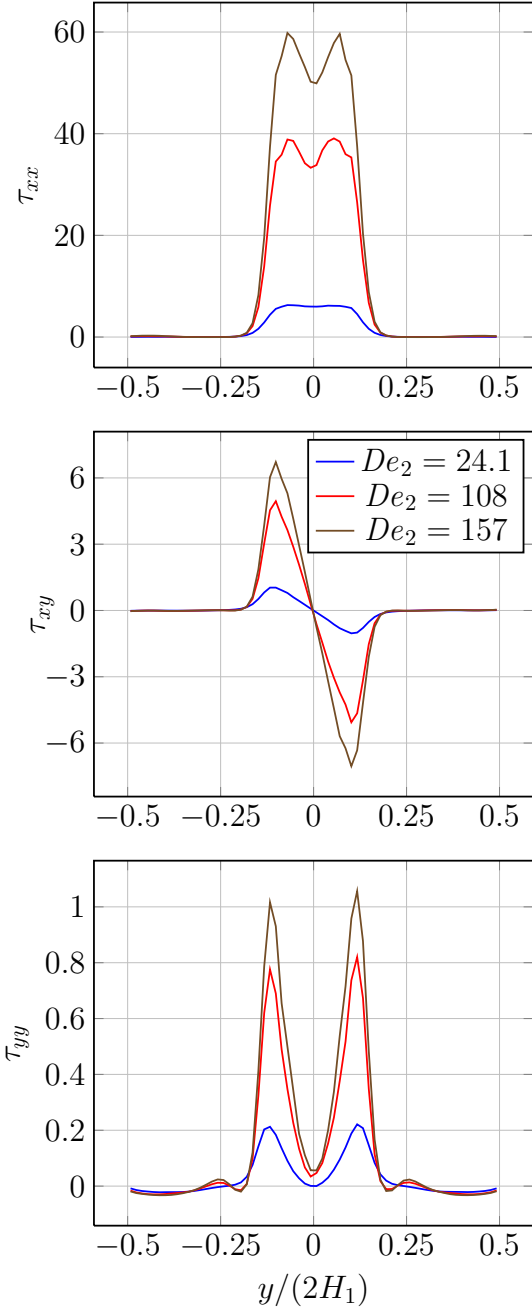


Figure 39: Steady state stress components τ_{xx} , τ_{xy} , and τ_{yy} in decreasing order of their magnitude.

τ_{xx} , τ_{xy} and τ_{yy} in decreasing order of magnitude over a vertical line given by $(-5/48, y/(2H_1), 0.5)$ with $y \in [-0.5, 0.5]$. As described before, the stress components have their maximum close to the corner singularity and are larger for the high Deborah number flows. Despite their different sizes, the stress maxima have the same physical position for each component. A consequence of the underlying stochastic process is that the components are not totally symmetric. Nevertheless, the stresses at steady state or at any fixed point in time are comparatively smooth compared to the time-dependent plots in Fig. 38.

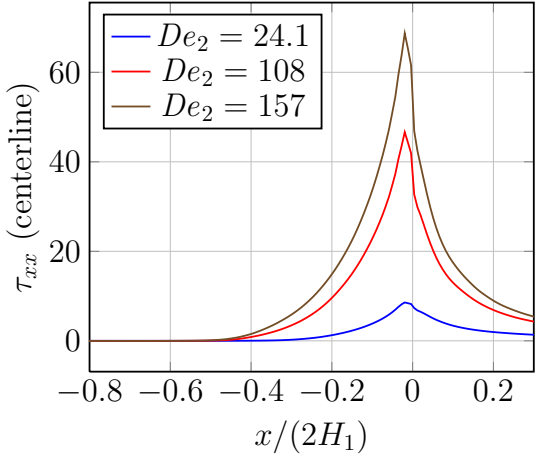


Figure 40: The plot illustrates τ_{xx} on the $2H_1$ -scaled horizontal centerline.

Fig. 40 displays τ_{xx} on the horizontal centerline. For a better analysis of the symmetry, the horizontal axis has been normalized with $2H_1$ and the axis has been shifted in its origin to coincide with the contraction center's origin. The τ_{xx} stress component starts to increase strongly at about $x/(2H_1) \approx -0.5$ for each of the considered Deborah numbers. This increase is delayed compared to the increase in the fluid velocity that begins at about $x/(2H_1) \approx -1$ as illustrated in Fig. 27 and Fig. 28. τ_{xx} reaches its maximum in the contraction and then starts to decrease.

5. Conclusion

3D square-square contraction flows were studied numerically for a multiscale FENE dumbbell model using the Brownian configuration field approach. Our implementation was validated, see Section 4.1, on a 2D Poiseuille flow for a Hookean dumbbell system and for the equivalent Oldroyd-B model. Both approaches, the Hookean dumbbell and the Oldroyd-B system, then reached the theoretically predicted rates of convergence of $1/2$ for the stochastic part and of 2 for the macroscopic flow variables in the considered problem. We also presented 2D contraction flow results for the FENE and FENE-P model and showed that both models significantly differ at steady state. From these results, we concluded that the FENE-P model does not deliver a good approximation to the FENE model for this kind of problem. Nevertheless, it would be interesting to investigate the differences between both models at steady state for the complex 3D flow. In Fig. 26 we presented 3D FENE-P simulation results in the early stage of the simulation and already observed noticeable deviations from the FENE model. We performed the 3D FENE-P simulations in the multiscale formulation and therefore the simulations could not be conducted up to a steady state due to the high computational effort. Presumably, macroscopic FENE-P simulations have to be combined with a

suitable stabilizing technique to avoid the issues caused by the high Weissenberg numbers involved.

The 3D simulations were compared with experimental measurements and showed an improved numerical stability compared to classical macroscopic methods. This coincides with literature findings for the BCF method, for instance by Mangoubi et al. [13]. With respect to the improved stability, multiscale methods are especially suited for situations in which elasticity is dominant and in which classical macroscopic approaches are restricted by the high Weissenberg number problem.

Our 3D contraction flow results exhibited a high agreement for low and moderate Weissenberg numbers but differed from the experimental measurements for flows with high elasticity. This discrepancy is not unexpected since the large computational requirements for the stochastic samples led to several limitations that might cause these differences:

- Alves et al. [47], among others, state that a single-mode model, such as the FENE dumbbell model, is not able to reproduce the shear and extensional flow behavior of actual polymer solutions over the whole range of experimental measurements. Instead, a multi-mode model with different relaxation times k for the relaxation spectrum λ_k is required. Each λ_k , combined with the corresponding viscosity contribution η_k , leads to an evolution equation for a dumbbell system as in (13). The stress tensor $\tau_{p,k}$ for each contribution k is then linearly superimposed. For most macroscopic approaches a multi-mode model does not increase the computation time particularly. However, for the multiscale approach this is no longer the case since the computational effort increases k times for a k -mode model.
- An approach that better describes the structure of a polymer, compared to a multi-mode model, is a multi-bead-spring FENE model. In this case, the molecule is approximated as a system of $k+1$ beads that are connected with k elastic springs. The corresponding Fokker-Planck equation (8) then has $3k$ -dimensions in configuration space and three dimensions in the flow space. Koppol et al. [21] simulated a 0.0025 wt % PS/PS Boger fluid in a planar 4:1:4 contraction-expansion flow with a dumbbell and with multi-bead-spring models. Even though the dumbbell and the three-spring FENE model were both in good agreement with the fluid at steady shear and in steady uniaxial extension, only the three-bead-spring model accurately modeled the pressure drop behavior at higher Deborah number flows. As mentioned before, the pressure drop enhancement is closely connected with the corner vortex dynamics. Koppol et al. show in [20] that their k -bead-spring model implementation scales linearly in the number of springs k .

- For the simulation of the three-dimensional contraction flow we decided for FENE $b = 20$ because the agreement was best for the steady shear flow material function. Since we are not aware of the material functions for an extensional flow, other choices for b might deliver a better general characterization of the experimental fluid. This becomes especially important since the size of the corner vortex considerably depends on b as illustrated in Fig. 26.
- The staggered finite difference grid uses the cell centers and the cell faces for storing the unknowns of the velocity, pressure and stress tensor field. Therefore, the corner singularity at the contraction is numerically resolved up to a distance of about half the mesh width and, consequently, the corner singularity is slightly regularized. As reported in the literature, for instance by Boger and Walters [48], a rounded corner in the contraction geometry reduces the resulting vortex size.
- As shown in Section 4.1, an increase in the number of Brownian configuration fields reduces the error in τ_p with a rate of $1/2$. A further limitation originated from the number of stochastic samples used in the simulations. With respect to a high accuracy in τ_p , the sample number per cell N_{BCF} should be of order $\mathcal{O}(10^6)$ or higher which is beyond the capabilities of current high performance computation.

Our results indicate the potential of multiscale methods for simulating real polymeric fluids. They avoid closure errors that are typical for macroscopic approaches and, at least in the case of the Brownian configuration field method, lead to a noticeable increase in numerical stability. However, multiscale simulations involve massively parallel computing for more complex 3D flow problems.

Acknowledgments

The authors wish to thank Dr. P.C. Sousa from University of Porto, Portugal, for fruitful discussions and for providing the steady state vortex lengths plotted in Fig. 24 and the experimental velocity profiles used in Fig. 27 and Fig. 28.

References

- [1] A. Peterlin, Hydrodynamics of macromolecules in a velocity field with longitudinal gradient, *J. Polym. Sci. B* 4 (1966) 287–291.
- [2] G. Lielens, R. Keunings, V. Legat, The FENE-L and FENE-LS closure approximations to the kinetic theory of finitely extensible dumbbells, *J. Non-Newtonian Fluid Mech.* 87 (1999) 179–196.
- [3] R. G. Owens, T. N. Phillips, *Computational Rheology*, volume 2, Imperial College Press, London, 2002.
- [4] P. Biller, F. Petruccione, The flow of dilute polymer solutions in confined geometries: a consistent numerical approach, *J. Non-Newtonian Fluid Mech.* 25 (1987) 347–364.

- [5] R. Keunings, Micro-macro methods for the multiscale simulation of viscoelastic flow using molecular models of kinetic theory, *Rheol. Rev.* (2004) 67–98.
- [6] R. B. Bird, C. F. Curtiss, R. C. Armstrong, O. Hassager, *Dynamics of Polymeric Liquids*, Kinetic Theory (Dynamics of Polymer Liquids Vol. 2), Wiley-Interscience, New York, 1987.
- [7] C. Chauvière, A. Lozinski, Simulation of dilute polymer solutions using a Fokker-Planck equation, *Comput. Fluids* 33 (2004) 687–696.
- [8] A. Lozinski, C. Chauvière, A fast solver for Fokker-Planck equation applied to viscoelastic flows calculations: 2D FENE model, *J. Comput. Phys.* 189 (2003) 607–625.
- [9] C. Chauvière, A. Lozinski, Simulation of complex viscoelastic flows using the Fokker-Planck equation: 3D FENE model, *J. Non-Newtonian Fluid Mech.* 122 (2004) 201–214.
- [10] D. J. Knezevic, E. Süli, A deterministic multiscale approach for simulating dilute polymeric fluids, in: *BAIL 2008-Boundary and Interior Layers*, Springer, 2009, pp. 23–38.
- [11] F. Chinesta, A. Ammar, A. Leygue, R. Keunings, An overview of the proper generalized decomposition with applications in computational rheology, *J. Non-Newtonian Fluid Mech.* 166 (2011) 578–592.
- [12] B. Mokdad, A. Ammar, M. Normandin, F. Chinesta, J. R. Clermont, A fully deterministic micro-macro simulation of complex flows involving reversible network fluid models, *Math. Comput. Simul.* 80 (2010) 1936–1961.
- [13] C. Mangoubi, M. Hulsen, R. Kupferman, Numerical stability of the method of Brownian configuration fields, *J. Non-Newtonian Fluid Mech.* 157 (2009) 188–196.
- [14] M. Laso, H. C. Öttinger, Calculation of viscoelastic flow using molecular models: the CONNFFESSIT approach, *J. Non-Newtonian Fluid Mech.* 47 (1993) 1–20.
- [15] A. Lozinski, R. G. Owens, T. N. Phillips, The Langevin and Fokker-Planck equations in polymer rheology, in: R. Glowinski, J. Xu (Eds.), *Numerical Methods for Non-Newtonian Fluids*, volume 16 of *Handbook of Numerical Analysis*, Elsevier, 2011, pp. 211 – 303.
- [16] M. A. Hulsen, A. P. G. Van Heel, B. H. A. A. Van Den Brule, Simulation of viscoelastic flows using Brownian configuration fields, *J. Non-Newtonian Fluid Mech.* 70 (1997) 79–101.
- [17] J. Bonvin, M. Picasso, Variance reduction methods for CONNFFESSIT-like simulations, *J. Non-Newtonian Fluid Mech.* 84 (1999) 191–215.
- [18] R. O. Vargas, O. Manero, T. N. Phillips, Viscoelastic flow past confined objects using a micro-macro approach, *Rheol. Acta* 48 (2009) 373–395.
- [19] J. L. Prieto, R. Bermejo, M. Laso, A semi-Lagrangian micro-macro method for viscoelastic flow calculations, *J. Non-Newtonian Fluid Mech.* 165 (2010) 120–135.
- [20] A. P. Koppol, R. Sureshkumar, B. Khomami, An efficient algorithm for multiscale flow simulation of dilute polymeric solutions using bead-spring chains, *J. Non-Newtonian Fluid Mech.* 141 (2007) 180–192.
- [21] A. P. Koppol, R. Sureshkumar, A. Abedijaberi, B. Khomami, Anomalous pressure drop behaviour of mixed kinematics flows of viscoelastic polymer solutions: a multiscale simulation approach, *J. Fluid Mech.* 631 (2009) 231–251.
- [22] K. D. Smith, A. Sequeira, Micro-macro simulations of a shear-thinning viscoelastic kinetic model: applications to blood flow, *Appl. Anal.* 90 (2011) 227–252.
- [23] J. Ramírez, M. Laso, Micro-macro simulations of three-dimensional plane contraction flow, *Modell. Simul. Mater. Sci. Eng.* 12 (2004) 1293–1306.
- [24] A. V. Bhate, R. C. Armstrong, R. A. Brown, Kinetic theory and rheology of dilute, nonhomogeneous polymer solutions, *J. Chem. Phys.* 95 (1991) 2988–3000.
- [25] J. C. Bonvin, Numerical simulation of viscoelastic fluids with mesoscopic models, Ph.D. thesis, École polytechnique fédérale de Lausanne, 2000.
- [26] M. Herrchen, H. C. Öttinger, A detailed comparison of various FENE dumbbell models, *J. Non-Newtonian Fluid Mech.* 68 (1997) 17–42.
- [27] J. Von Neumann, Various techniques used in connection with random digits, *Appl. Math Ser.* 12 (1951) 36–38.
- [28] M. Griebel, T. Dornseifer, T. Neunhoeffer, *Numerical Simulation in Fluid Dynamics, a Practical Introduction*, SIAM, Philadelphia, 1998.
- [29] R. Croce, M. Griebel, M. A. Schweitzer, Numerical simulation of bubble and droplet-deformation by a level set approach with surface tension in three dimensions, *Int. J. Numer. Methods Fluids* 62 (2009) 963–993.
- [30] G. S. Jiang, C. W. Shu, Efficient implementation of weighted ENO schemes, *J. Comput. Phys.* 126 (1996) 202–228.
- [31] S. Claus, Numerical simulation of unsteady three-dimensional viscoelastic Oldroyd-B and Phan-Thien Tanner flows, Diplomarbeit, Institut für Numerische Simulation, Universität Bonn, 2008.
- [32] J. B. Bell, P. Colella, H. M. Glaz, A second-order projection method for the incompressible Navier-Stokes equations, *J. Comput. Phys.* 85 (1989) 257–283.
- [33] B. Verleye, M. Klitz, R. Croce, D. Roose, S. Lomov, I. Verpoest, Computation of the permeability of textiles with experimental validation for monofilament and non crimp fabrics, in: *Computational Textile*, volume 55 of *Studies in Computational Intelligence*, Springer Berlin / Heidelberg, 2007, pp. 93–110.
- [34] H. C. Öttinger, *Stochastic Processes in Polymeric Fluids: Tools and Examples for Developing Simulation Algorithms*, Springer, Berlin, 1996.
- [35] B. F. Smith, P. E. Bjørstad, W. Gropp, *Domain Decomposition: Parallel Multilevel Methods for Elliptic Partial Differential Equations*, Cambridge University Press, Cambridge, 2004.
- [36] R. Croce, M. Griebel, M. A. Schweitzer, A parallel level-set approach for two-phase flow problems with surface tension in three space dimensions, Preprint 157, Sonderforschungsbereich 611, Universität Bonn, 2004.
- [37] M. Melchior, H. C. Öttinger, Variance reduced simulations of polymer dynamics, *J. Chem. Phys.* 105 (1996) 3316–3331.
- [38] N. D. Waters, M. J. King, Unsteady flow of an elastico-viscous liquid, *Rheol. Acta* 9 (1970) 345–355.
- [39] E. O. Carew, P. Townsend, M. F. Webster, Taylor-Galerkin algorithms for viscoelastic flow: application to a model problem, *Numerical Methods for Partial Differential Equations* 10 (1994) 171–190.
- [40] P. Wapperom, R. Keunings, V. Legat, The backward-tracking Lagrangian particle method for transient viscoelastic flows, *J. Non-Newtonian Fluid Mech.* 91 (2000) 273–295.
- [41] P. C. Sousa, P. M. Coelho, M. S. N. Oliveira, M. A. Alves, Effect of the contraction ratio upon viscoelastic fluid flow in three-dimensional square-square contractions, *Chem. Eng. Sci.* 66 (2011) 998–1009.
- [42] P. C. Sousa, P. M. Coelho, M. S. N. Oliveira, M. A. Alves, Three-dimensional flow of Newtonian and Boger fluids in square-square contractions, *J. Non-Newtonian Fluid Mech.* 160 (2009) 122–139.
- [43] F. M. White, *Viscous Fluid Flow*, McGraw-Hill, New York, 1991.
- [44] R. Keunings, On the high Weissenberg number problem, *J. Non-Newtonian Fluid Mech.* 20 (1986) 209–226.
- [45] R. Fattal, R. Kupferman, Constitutive laws for the matrix-logarithm of the conformation tensor, *J. Non-Newtonian Fluid Mech.* 123 (2004) 281–285.
- [46] M. A. Alves, P. J. Oliveira, F. T. Pinho, Benchmark solutions for the flow of Oldroyd-B and PTT fluids in planar contractions, *J. Non-Newtonian Fluid Mech.* 110 (2003) 45–75.
- [47] M. A. Alves, F. T. Pinho, P. J. Oliveira, Viscoelastic flow in a 3D square/square contraction: visualizations and simulations, *J. Rheol.* 52 (2008) 1347–1368.
- [48] D. V. Boger, K. Walters, *Rheological Phenomena in Focus*, Elsevier, Amsterdam, 1993.